J. Fluid Mech. (2025), *vol.* 1024, A22, doi:10.1017/jfm.2025.10914

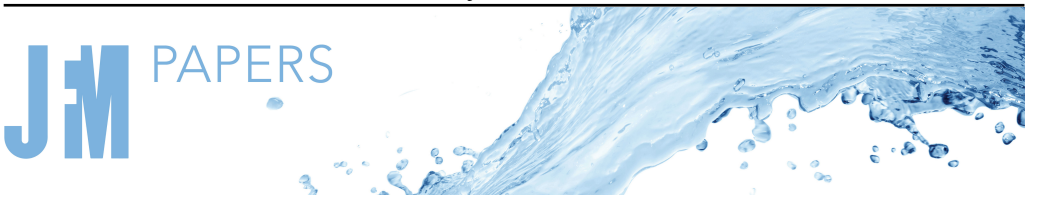

Vortex topology in the lee of a 6 : 1 prolate spheroid

Marc Plasseraud[1] **and Krishnan Mahesh**[1]

[1]Naval Architecture and Marine Engineering, University of Michigan, Ann Arbor, MI 48109, USA

Corresponding author: Krishnan Mahesh, krmahesh@umich.edu

(Received 22 May 2025; revised 25 September 2025; accepted 28 October 2025)

A large-scale parametric study of the flow over the prolate spheroid is presented to understand the effect of Reynolds number and angle of attack on the separation, the wake formation and the loads. Large-eddy simulation is performed for six Reynolds numbers ranging from $Re = 0.15 \times 10^6$ to 4×10^6 and for eight angles of attack ranging from $\alpha = 10°$ to $\alpha = 90°$. For all the cases considered, the boundary layer separates symmetrically and forms a recirculation region. Several distinct flow topologies are observed that can be grouped into three categories: proto-vortex, coherent vortex and recirculating wake. In the proto-vortex state, the recirculation does not have a distinct centre of rotation, instead, a two-layer detached flow structure is formed. In the coherent vortex state, the separated shear layer rolls into a three-dimensional vortex that is aligned with the axis of the spheroid. This vortex has a clear centre of rotation corresponding to a minimum of pressure and transforms the transverse momentum from the separated shear layer into axial momentum. In the recirculating wake regime, the recirculation is incoherent and the primary separation forms a dissipative shear layer that is convected in the direction of the free stream. This symmetric pair of shear layers bounds a low-momentum recirculating cavity on the leeward side of the spheroid. The properties of these states are not constant, but evolve along the axis of the spheroid and are dictated by the characteristics of the boundary layer at separation. The variation of the flow with Reynolds number and angle of attack is described, and its connection to the loads on the spheroid are discussed.

Key words: boundary layer separation, turbulence simulation, vortex dynamics

1. Introduction

The phenomena of flow separation and vortex formation affect a wide variety of external flows, including marine and aerial vehicles. Whether boundary layer separation is detrimental (airfoil stall) or desired (delta wing), these effects dominate the loads. Thus, a correct understanding of the physics of separation and recirculation is critical to predict vehicle performance and manoeuvrability. To that end, past work has studied the flows over spheres (Taneda 1956; Johnson & Patel 1999), cylinders (Williamson 1996), elliptic cones (Crabbe 1965), delta wings (Brown Jr. & Michael 1954; Lee & Ho 1990) and SUBOFF (Kumar & Mahesh 2018; Morse & Mahesh 2021).

The 6 : 1 prolate spheroid is one such canonical streamlined body. Despite its geometrical simplicity, the spheroid generates a wide array of complex flow features such as streamline curvature, cross-flow transition, three-dimensional (3-D) separations and large recirculating flow structures. This complexity makes it a particularly attractive canonical problem for evaluating numerical models, e.g. Constantinescu *et al.* (2002), Rhee & Hino (2002), Scott & Duque (2004), Wikström *et al.* (2004), Xiao *et al.* (2007) and Fureby & Karlsson (2009).

When the spheroid is inclined to the flow, a 3-D boundary layer (Cebeci & Meier 1987) forms on the windward side. The three-dimensionality is a consequence of streamline curvature and is characterized by a secondary flow, as described experimentally by Chesnakas & Simpson (1994). Multiple pathways of turbulent transition exist in the boundary layer, including Tollmien–Schlichting, separation line, attachment line and cross-flow instabilities (Rubino 2021). The interaction between these modes makes the boundary layer challenging to resolve adequately, and predicting transition on the spheroid is still an area of active research. The importance of predicting transition of the attached flow is notable because the state of the boundary layer strongly influences the location of separation, which, in turn, leads to changes in the topology of the recirculation and the loads (Hedin *et al.* 2001; Constantinescu *et al.* 2002). The spheroid is often artificially tripped in experiments and simulations. The purpose of the trip is to bypass natural transition and to generate a turbulent boundary layer, thereby ensuring repeatability and behaviour representative of a full-scale model. There are indications that the presence of a trip does not guarantee that the boundary layer becomes turbulent, particularly at higher incidence (Plasseraud, Kumar & Mahesh 2023). The transition of the boundary layer from laminar to turbulent at separation leads to the existence of a critical Reynolds number between $Re = 2 \times 10^6$ and $Re = 3 \times 10^6$ (Ahn 1992) for an angle of attack $\alpha \leqslant 20°$. This transition is accompanied by changes in the location of separation, the size and vorticity of the recirculation and the suction exerted on the spheroid. In addition, the primary vortex is attached and coherent at low angles of attack (10°, 20°), while a wake forms at 90°, without a visible coherent vortical structure (El Khoury, Andersson & Pettersen 2010).

The recirculation has been extensively studied at 10° and 20° in the subcritical (Guo, Kaiser & Rival 2023), critical (Ahn 1992) and supercritical regime (Chesnakas & Simpson 1994, 1997). The latter study offers particularly detailed measurements of velocity profiles, wall flow angle, turbulent quantities and velocity perturbation correlations in the boundary layer and around the primary vortex. Fewer studies have looked at higher incidences. Jiang, Gallardo & Andersson (2014) performed direct numerical simulations (DNS) of the flow for an incidence of 45° at $Re \leqslant 1000$, and observed an unusual port/starboard asymmetry of the vortex pair despite the symmetry of the problem. El Khoury *et al.* (2010, 2012) performed DNS at $Re = 1 \times 10^5$ in the laminar regime at $\alpha = 90°$. The choice of this

incidence had not been investigated prior to these publications, and it reveals interesting similarities to the flow around a cylinder.

The origin of the loads on the spheroid is a topic of particular importance and has been studied both numerically and experimentally. Du & Zaki (2025) characterized the loads on the prolate spheroid in terms of the Josephson–Anderson relation (Josephson 1965; Anderson 1966) which connects the vorticity flux to the drag on the body. Fu *et al.* (1994) specifically studied the effect of Re/α on the spheroid flow for small to moderate incidences around the critical Reynolds number. Their experimental study mainly investigated the origin of the force, its connection to the circulation in the primary vortex and its evolution with varying Re/α. They note that the circulation of the vortex increases with increasing angle of attack, while increasing Re moves the separation leeward. More generally, the suction force generated by the recirculation can be treated in terms of the vortex impulse as formulated by Truesdell (1954) and Saffman (1995), and applied by Wu, Lu & Zhuang (2007).

Plasseraud *et al.* (2023) performed wall-resolved, trip-resolved large-eddy simulation (LES) on the prolate spheroid at 10° and 20°, for a Reynolds number $Re = 4.2 \times 10^6$. They focused on the windward, attached boundary layer and recorded the velocity components, the turbulent stresses and the production of turbulent kinetic energy (TKE) along two attached streamlines. They concluded that the state of the attached boundary layer was influenced by the streamline curvature effects, which in turn affected the separation and the loads on the spheroid. The purpose of the present study is to relate the nature of separation and changes in the topology of the recirculation to the loads on the spheroid. Towards this goal, a large number of simulations (48) have been performed on a range of Reynolds numbers and angles of incidence varying from $Re = 0.15 \times 10^6$ to $Re = 4 \times 10^6$ and an angle of attack ranging from $\alpha = 10°$ $\alpha = 90°$. This study provides, to the best of our knowledge, the most expansive set of numerical data on the spheroid.

The paper is organized as follows: §§ 2 and 3 describe the LES solver used and the methodology used to predict the location of separation, the vortex boundary and the boundary layer thickness; § 4 details the grid convergence study; § 5 discusses the results. After an overview of the flow, the evolution of the recirculation with (α, Re) is characterized. It is then shown that the properties of the recirculation evolve in the axial direction in a predictable fashion that can be collapsed for most (α, Re) pairs. Finally, the normal force and pitching moments are discussed in relation with the observed flow behaviours. Section 6 concludes the paper.

2. Numerical method

The overbar $\overline{(\cdot)}$ denotes spatial filtering and the bracket $\langle\cdot\rangle$ indicates time averaging. The incompressible, spatially filtered Navier–Stokes equation are solved in a LES formulation,

$$\frac{\partial \overline{u}_i}{\partial t} + \frac{\partial}{\partial x_j}(\overline{u}_i \overline{u}_j) = -\frac{\partial \overline{P}}{\partial x_i} + \nu \frac{\partial^2 \overline{u}_i}{\partial x_j \partial x_j} - \frac{\partial \tau_{ij}}{\partial x_j}, \tag{2.1}$$

$$\frac{\partial \overline{u}_i}{\partial x_i} = 0, \tag{2.2}$$

where u_i is the velocity, P is the pressure divided by density and ν is the kinematic viscosity. The subgrid stress $\tau_{ij} = \overline{u_i u_j} - \overline{u}_i \overline{u}_j$ is modelled with the dynamic Smagorinsky model (Germano *et al.* 1991; Lilly 1992). A finite volume, second-order centred spatial discretization is used where the filtered velocity components and pressure are stored at the cell-centroids while the face-normal velocities are estimated at the face centres.

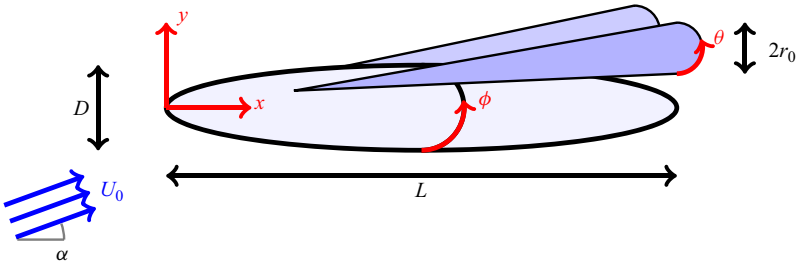

Figure 1. Schematic of the body-oriented coordinate systems.

The equations are marched in time with a second-order Crank–Nicolson scheme. The algorithm has shown good performance for multiple complex flows, such as propeller flows (Verma & Mahesh 2012; Kroll & Mahesh 2022; Leasca, Kroll & Mahesh 2025) and flows over hulls (Kumar & Mahesh 2018; Morse & Mahesh 2021). The kinetic-energy conservation property of the method (Mahesh, Constantinescu & Moin 2004) makes it suitable for high Reynolds number flows such as the one presented in this paper. The method was extended by Horne & Mahesh (2019*a*,*b*) to allow for overlapping (overset) grids and six-degree of freedom movement. Although the present geometry is stationary, overset grids are used for better grid efficiency by circumventing the need for a one-to-one match between the near-wall region and the far-field. In addition, overset grids provide more flexibility in the grid generation process as they allow for the refinement of specific areas of the flow such as the vortex region in the current study.

3. Methodology

3.1. *Notations*

The angle of attack is denoted by α and Re is the Reynolds number based on the major length L of the spheroid and free stream velocity U_0. Note that all variables indicated are non-dimensioned by U_0, L and ρ. The azimuthal angle with respect to the spheroid is written as ϕ, where $\phi = 0°$ corresponds to the windward (i.e. pressure side) meridian and $\phi = 180°$ is the leeward (i.e. suction side) meridian. On the $\phi \in [0°, 180°]$ side, the primary and tertiary vortices (if they are present) rotate anticlockwise with respect to the axis of the spheroid, while the secondary vortex rotates clockwise. The direction of rotation of all three types of vortices is opposite on the other side ($\phi \in [180°, 360°]$). Here $\boldsymbol{u}$ and $\boldsymbol{\omega}$ are the velocity and vorticity vector, normalised by U_0 and U_0/L, respectively, in the body-oriented reference frame. Following these conventions, the helicity density $\boldsymbol{u} \cdot \boldsymbol{\omega}/(\|\boldsymbol{u}\|\|\boldsymbol{\omega}\|)$ is negative in the primary vortex and positive in the secondary vortex for $\phi \in [0°, 180°]$. If the primary vortex is detected, it has radius r_0, circulation $\Gamma_v = \int_v \omega_x \mathrm{d}v$, an area A_v and azimuthal angle θ.

3.2. *Coordinate system*

An angle of attack α is considered with respect to the major axis of the spheroid. Two coordinate systems are used and displayed in figure 1. The first is Cartesian and originates at the nose of the spheroid. The x axis is aligned with the major axis of the spheroid and is referred to as the 'axial' coordinate. Here $x/L = 0$ is the nose and $x/L = 1$ is the tail end of the spheroid. The y axis also rotates with the spheroid; its coordinate is negative on the windward side and positive on the leeward side such that y aligns with the free stream velocity vector when $\alpha = 90°$. The z axis corresponds to the spanwise direction.

The meridian plane will be referred to as the plane for which $z = 0$. The second coordinate system is also body-oriented and cylindrical. The azimuthal direction ϕ is zero on the windward meridian and 180° on the leeward meridian. The radial direction r is orthogonal to the x and ϕ axes; it is zero on the wall of the spheroid and increases with distance from the wall. The body-oriented reference frame is used unless otherwise specified.

3.3. *Statistics measurement*

The transient development of the flow has been observed to last approximately one length flow-through $t \approx L/U_0$ with small variations depending on the incidence. The flow is computed for $t = 2L/U_0$ to wash out transients, then averaged for a duration of $t = 3L/U_0$. Time-averaged variables are denoted as $\langle . \rangle$.

3.4. *Location of separation*

Past experiments and simulations have used the minimum magnitude of skin friction as an indicator of the location of primary separation. Although this metric is convenient and satisfactory at low angles of attack, it is an imprecise metric (Chesnakas & Simpson 1996) and can, at higher angles of attack, lead to false positives. Another approach is to locate the line of separation as the line of convergence of friction lines. This was done by Kim, Rhee & Cokljat (2003) and Morrison *et al.* (2003) to locate the separation and reattachment lines on the spheroid. Although this method yields good results for visual identification, the line of convergence is difficult to locate numerically. Instead, Moffatt & Tsinober (1992) have suggested that the helicity density defined as $h = \boldsymbol{u} \cdot \boldsymbol{\omega}$ switches sign across a 3-D separation. This method was also suggested by Levy, Degani & Seginer (1990) to visualize 3-D separations and recirculation. Chesnakas & Simpson (1996) observed this fact in the case of the spheroid at $\alpha = 10°, 20°$. The helicity density metric is used in the current study, since it was observed to be a reliable indicator of the separation locations for each of the cases studied. Figure 2 shows time-averaged skin friction coefficient at $\alpha = 60°$ and $Re = 4 \times 10^6$, along with the lines of minimal $\langle c_f \rangle$ (red lines) and the location at which the helicity density switches sign (turquoise markers). In this case, there are several minima of $\langle c_f \rangle$, some of which are not associated with boundary layer separation. The presence of several minimal lines make it difficult to algorithmically identify the one associated with the primary separation. In addition, the variations of $\langle c_f \rangle$ with ϕ are small close to separation, which can yield a large error in locating the location of the minimum point. The azimuthal location where helicity density is zero on the other hand, is close to where the wall intersects the direction of the separated shear layer; it is also close to the point where the transverse velocity switches sign. Note that even though the sign of transverse velocity is a good indicator of separation at high angle of attack where the separation is more two-dimensional (2-D), it is not a good metric at low angle of attack where flow separation can occur without sign reversal. The symbol ϕ_s is used to indicate the azimuthal location of the separation throughout this study.

3.5. *Identification of recirculation region*

The domain of recirculation is challenging to assess. A similar methodology as Griffin, Fu & Moin (2021) can be used to identify the recirculation region based on a threshold of stagnation pressure. Two options were considered to determine the stagnation pressure threshold to be consistent with the δ_{99} definition. First, the threshold could be taken as the stagnation pressure value at $r = \delta_{99}$. However, this is potentially sensitive to uncertainty in the measurement of boundary layer thickness. Second, since we have

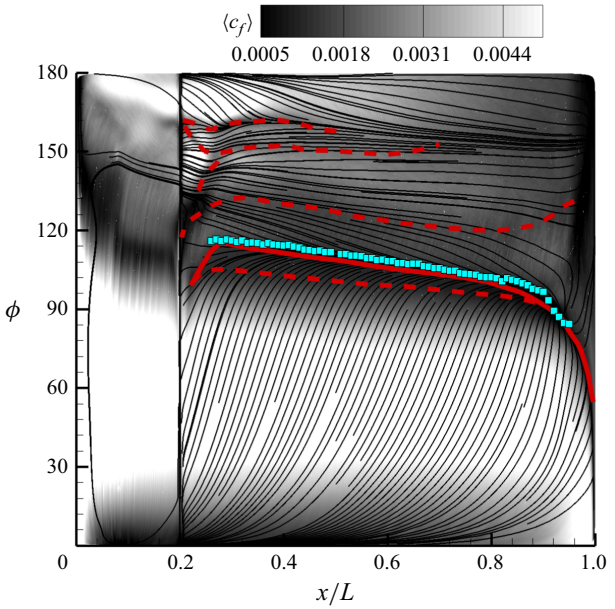

Figure 2. Time-averaged skin friction coefficient at $\alpha = 60°$ and $Re = 4 \times 10^6$. The turquoise markers represent the locations of primary separation predicted from helicity, the continuous red line the primary separation from the azimuthal minimum of $\langle c_f \rangle$, the dotted red lines represent lines of minimum $\langle c_f \rangle$ that are not at the primary separation. The dotted red lines at $\phi \approx 150°$ and $\phi \approx 160°$ are located at the secondary separation, all other dotted red lines are spurious and not on a location of separation. The friction lines are drawn in black. Convergence of friction lines is indicative of separation, divergence of friction lines is indicative of flow attachment.

$\boldsymbol{u} \cdot \boldsymbol{u}/u_p^2 = \boldsymbol{u} \cdot \boldsymbol{u}/(2(P_s^\infty - P)) = 0.99^2$, the following threshold on P_s could be imposed:

$$P_s = P(1.0 - 0.99^2) + 0.99^2 P_s^\infty \approx 0.49 P_s^\infty. \tag{3.1}$$

Thus, for any transverse location x/L where separation occurs, the separated region is defined as the area where $P_s < 0.49 P_s^\infty$ and $r > \delta_{99}$. This methodology is easy and leads to a definition consistent with that of the boundary layer thickness.

3.6. *Identification of primary vortex boundary*

Identifying the boundary of the primary vortex is difficult for similar reasons as the measurement of the boundary layer and the determination of the recirculation region. To be viable for the present study, a method must be fast enough to run on a large set of data, be robust to be applied to a wide variety of vortex topologies, be physically consistent and provide additional information such as centre of the vortex and reliable circulation estimates. Two common methods were initially considered. The first method was to define the boundary of the vortex as $\lambda_2 = 0$, where λ_2 is the second invariant of velocity, as proposed by Jeong & Hussain (1995). Although the λ_2 method is commonly used to visualize vortices, the $\lambda_2 = 0$ boundary is very sensitive to noise and therefore unreliable to use for integral calculations. The second method considered was to impose a threshold on vorticity and the centre of the vortex. Assuming a Gaussian profile of vorticity, the vortex boundary can be taken as the line where $\omega_x = \omega_0/e$, where ω_0 is the vortex centre vorticity and e is Euler's number. Although simple, this method gave poor results on the current data set because not all vortices had a Gaussian profile.

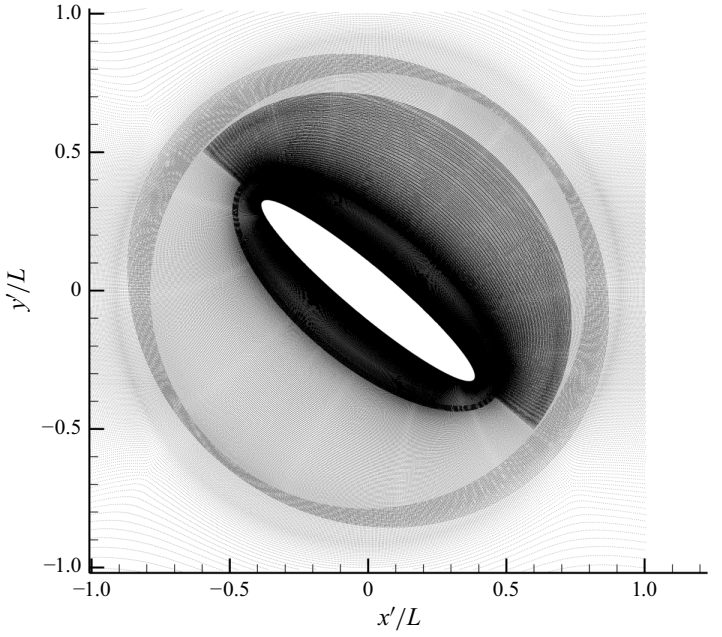

Figure 3. Longitudinal view of the fine grid in a free stream based coordinate system (x', y', z'). The dots represent the location of the cell centres. Four overset levels are visible: the coarser and outermost is referred to as level 0, followed by level 1 and level 2, the closest to the wall of the spheroid. The fourth overset grid is visible on the leeward side of the flow only.

To address these limitations, Plasseraud & Mahesh (2024*a*) devised a novel method, which defines the vortex as the largest closed isosurface of stagnation pressure. This method was found to perform remarkably well on the wide range of flows that were studied and is used to analyse the results in the current study.

3.7. *Effects of tripping*

The boundary layer is tripped at $x/L = 0.2$ in order to better reproduce the conditions of past experimental campaigns (Ahn 1992; Chesnakas & Simpson 1994; Fu *et al.* 1994; Chesnakas & Simpson 1996; Wetzel 1996). The purpose of the trip is to artificially induce a turbulent boundary layer, thereby improving repeatability. Despite its common use, there are questions concerning the efficacy of the trip: the simulations of Aram *et al.* (2021, 2022) found that the trip did not produce a turbulent boundary layer at $\alpha = 20°$. Plasseraud *et al.* (2023) performed LES to compare cases with and without trip at $\alpha = 10°$, 20° and $Re = 4.2 \times 10^6$, and concluded that the tripping was successful at 10° but not at 20°, resulting in similar tripped and untripped flows.

4. Grid convergence

Three grid sizes are considered: 94×10^6, 218×10^6 and 470×10^6. All three grids have the same topology and only differ in the number of cells. The grids are composed of four different overset blocks used to refined the near-wall and the leeward regions.

Figure 3 shows a longitudinal view of the fine grid. Several overset refinements are used to circumvent the need for a 1 : 1 cell count between the wall of the spheroid and the far-field, improving grid efficiency. The cell size ratio between two overlapping grids ranges between 1.5 and 2. At high angle of attack ($\alpha > 40°$), the primary vortex pair is farther

Grid size	94×10^6	218×10^6	470×10^6
Fy	0.413	0.419	0.419

Table 1. Normal force Fy (force in the y-direction) on the three grids considered.

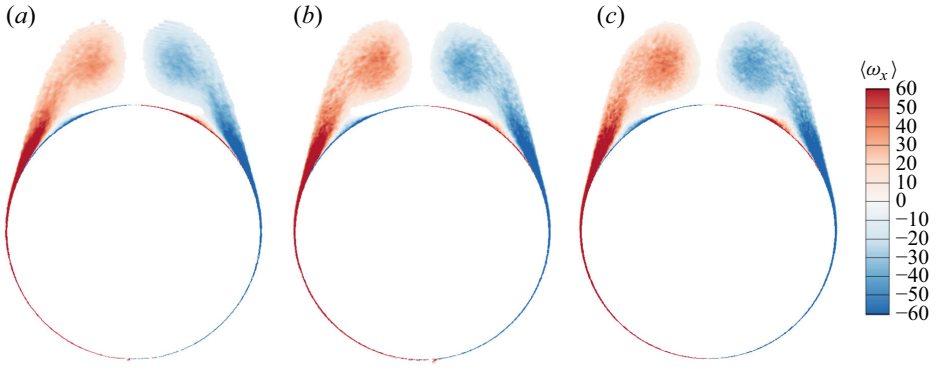

Figure 4. Time-averaged axial vorticity in a transverse section at $x/L = 0.8$, $\alpha = 20°$, $Re = 4 \times 10^6$ for the (a) coarse grid, (b) medium grid and (c) fine grid.

from the wall and can be in a coarser overset level. For this reason, an additional grid with a triangular cross-section is placed to obtain adequate resolution of the vortex regardless of incidence.

The convergence study is performed by comparing the normal force and the time-averaged flow field at $\alpha = 20°$ and $Re = 4 \times 10^6$. Table 1 shows the time-averaged normal force for the three grids. It is larger for the coarse grid and at close levels for the medium and fine grids. This suggests that the medium grid is sufficient to capture the physics of the flow. Figure 4 shows the axial vorticity for the three grids at $x/L = 0.8$. All three grids show a very similar flow composed of a primary separation leading to a primary vortex and a secondary, weaker separation. The vorticity in the centre of the vortex increases with increasing refinement, albeit to a lesser extent from the medium to the fine grid. Figure 5 shows the skin friction coefficient c_f on the wall of the spheroid for the three grids. For all three grids, the primary and secondary separations are visible as minima of c_f and a convergence of friction lines. In addition, perturbations are visible in the skin friction for all three grids. The perturbations have higher frequencies for the medium and fine grids compared with the coarse grid. The fine grid shows a slightly better definition of both separation lines and is the one used for this study.

5. Results and discussion

Figure 6 shows a perspective view of the time-averaged flow at $Re = 2 \times 10^6$ and $\alpha = 50°$. The boundary layer separates for the first time on the side of the spheroid. The separated shear layer then travels away from the wall and rolls up to form the primary recirculation. A secondary separation is also seen below the primary vortex, which leads to a secondary vortex pair, rotating in the opposite direction. The area of recirculation increases monotonically with x/L, increasing faster closer to the tail. The maximum axial vorticity decreases from the midbody to the tail of the spheroid as the area of recirculation

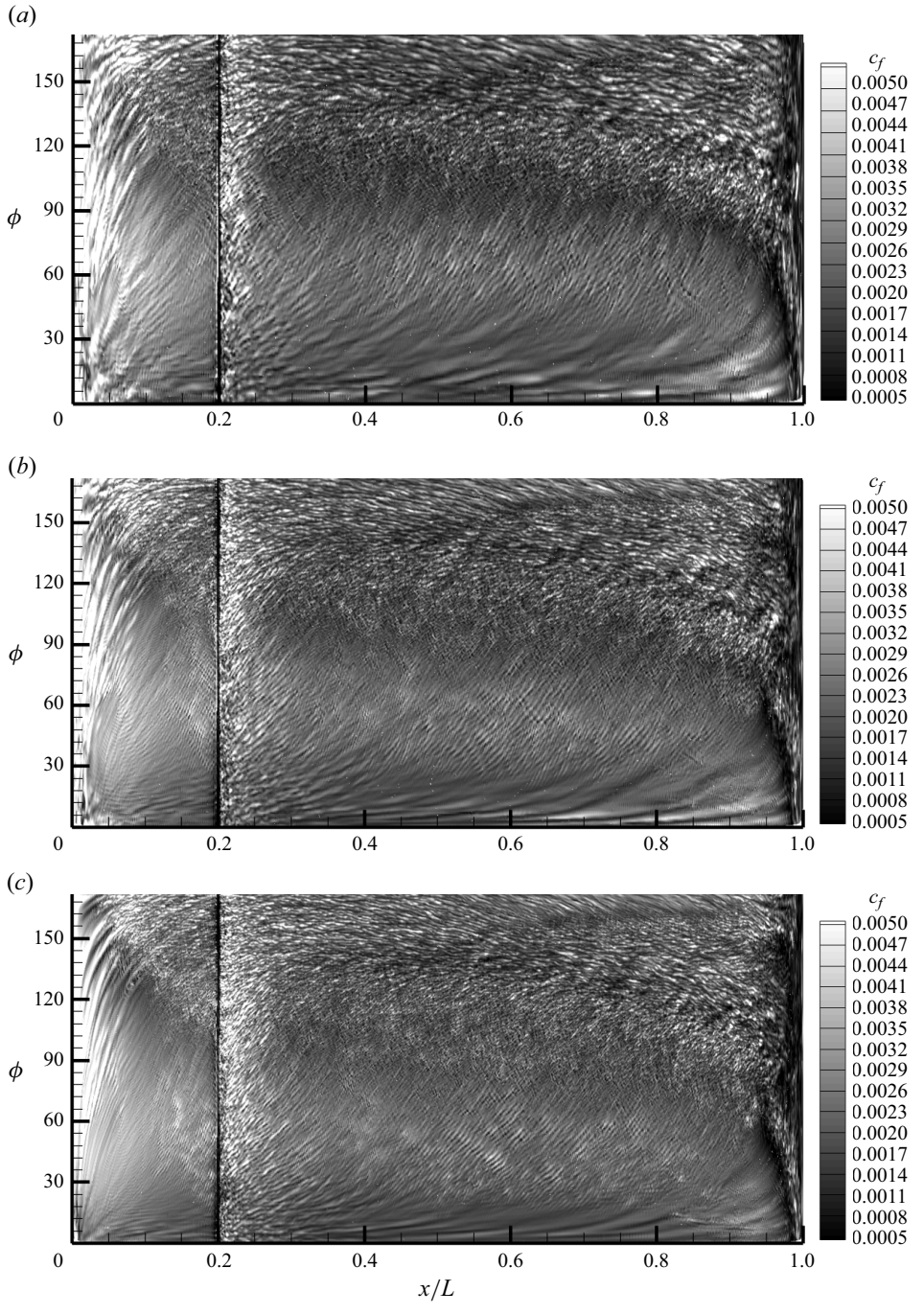

Figure 5. Skin friction coefficient versus x/L and ϕ at $\alpha = 20°$, $Re = 4 \times 10^6$ for the (*a*) coarse grid, (*b*) medium grid and (*c*) fine grid.

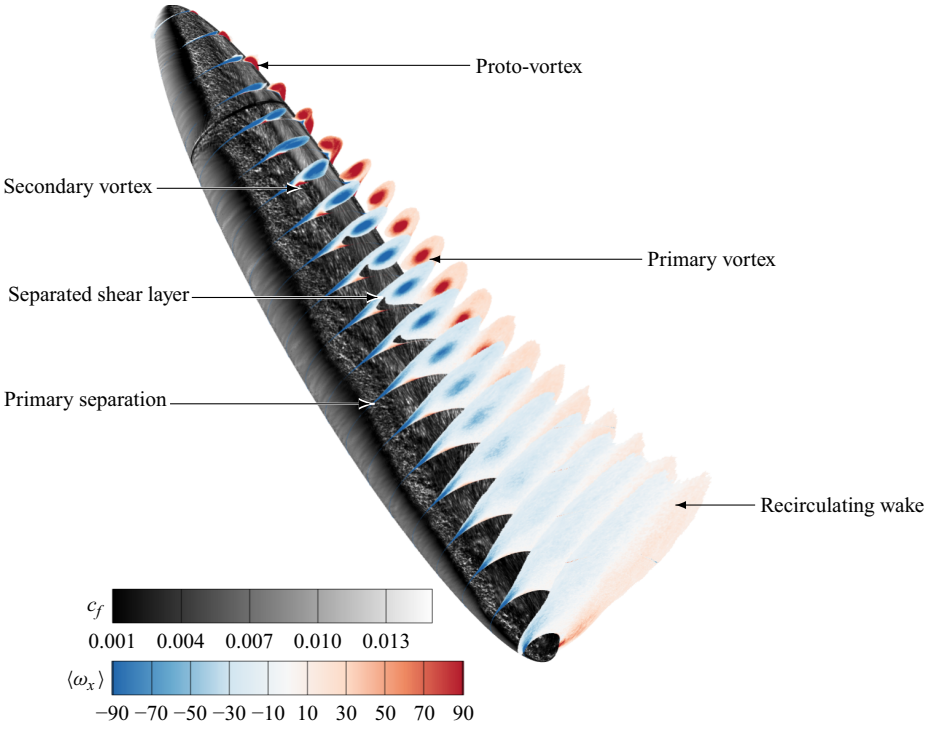

Figure 6. Perspective view of the flow around the spheroid at $Re = 2 \times 10^6$ and $\alpha = 50°$. The surface of the spheroid is coloured by instantaneous skin friction coefficient, the transverse slices are from $x/L = 0.025$ to $x/L = 0.975$ by a $\Delta x = 0.05L$ increment, and are coloured by time-averaged axial vorticity. The direction of flow is horizontally from left to right and out of the page.

increases. The secondary vortex also decays from the midbody, to disappear by the tail of the spheroid. The primary recirculation can be classified into one of three categories, depending on the axial coordinate x/L: proto-vortex close to the nose, followed by a coherent 3-D vortex in the midbody, evolving into a recirculating wake close to the tail of the spheroid. The subsequent results will show that these states are generalisable to the other pairs of Re and α. After a description of these states, it will also be shown that the evolution of the flow is related to changes at separation and that this evolving recirculation influences the loads on the spheroid.

5.1. *Overview*

The time-averaged axial vorticity at $x/L = 0.5$ is shown in figure 7, for all the calculated flows, sorted from left to right by increasing values of Reynolds number, and from bottom to top by increasing values of angle of attack. All the cases shown are symmetric and have at least one boundary layer separation, which leads to a recirculation. The topology of the recirculation varies and is affected by the angle of attack, the Reynolds number and the x/L location. The predominant effect of the angle of attack is to increase the size of the recirculation. From $\alpha = 10°$ to 50°, the recirculation consists of one to several pairs of vortices of increasing vorticity. At $\alpha = 70°$, the vorticity decreases although the recirculation is still bounded. At $\alpha = 90°$, the recirculation area is unbounded. The Reynolds number also alters the recirculation, albeit differently. The primary separation line moves leeward with increasing Reynolds number. This results in a closing of the separation angle and a shrinking of the primary separation. This effect is small at $\alpha = 10°$

and 20°, although more pronounced from 30° to 90°. These physical phenomena are detailed in later sections.

Figure 8 shows the skin friction coefficient c_f versus x/L and ϕ sorted from left to right by increasing Reynolds number, and from bottom to top by increasing angle of attack. Two main regions are visible that are separated by a line of minimum c_f. This line slopes and is increasingly horizontal with increasing α. The minimum c_f line meanders at $Re = 1 \times 10^6$ and is increasingly straight with increasing Re. Windward of this line, the flow is attached and has a uniform, high value of c_f for lower Re and higher α. This is indicative of a laminar boundary layer before separation. Leeward of the minimum c_f line, c_f is not uniform, indicative of an unsteady boundary layer. From $\alpha = 20°$ to $\alpha = 70°$, a second minimum c_f line is visible in the $\phi \in [160°, 180°]$ region. This second line is associated with the secondary separation of the boundary layer. On all c_f maps, the region between the leeward meridian $\phi = 180°$ and the secondary separation is smoother than the region between the primary and secondary separations. That region is located below the primary vortex and the separated lobe. Small transverse flow and large axial flow are observed in this region (see § 5.5.1). Transverse perturbations are visible, with higher frequencies for the higher Reynolds number than the lower Reynolds numbers. These perturbations correlate with unsteady axial changes in the primary vortex.

5.2. *Separation*

5.2.1. *Separation line*

For each case studied, the boundary layer detaches at least once and up to three times for the lower Reynolds number cases. The primary separation leads to the formation of a recirculation that is described in § 5.3. The present section aims to characterise the separation to better understand the behaviour of the recirculation.

Figure 9 shows the location of the primary separation for all the cases. For low angles of attack, no separation occurs until higher axial locations. The start of the primary separation moves towards lower axial locations as the angle of attack increases. In addition, the azimuthal position of the primary separation decreases with the axial position almost linearly between $x/L = 0.3$ and $x/L = 0.8$. This linear variation of the separation is also observed in experiments of Barber & Simpson (1990) and Fu *et al.* (1994). In addition, Fu *et al.* (1994) notes that increasing Re leads to delayed separation in the subcritical regime (defined by Fu *et al.* (1994) as $Re < 1.3 \times 10^6$), as measured in the present data.

The slope of the separation lines for all the cases is shown in figure 10. The separation line slope varies little with the Reynolds number but increases linearly with the angle of attack for $\alpha > 10°$. At $\alpha = 90°$, the slope separation line is zero, i.e. the azimuth of separation is independent of x/L. This is expected because of the symmetry in x at this angle, considering a negligible effect of the asymmetry introduced by the trip. The Reynolds number has an overall negligible effect on the slope of the separation.

While the angle of attack affects the slope of the separation line, Re affects its mean position. For all angles of attack, the average position of the separation increases with the Reynolds number until $Re = 3 \times 10^6$ and is constant for most incidences between $Re = 3 \times 10^6$ and $Re = 4 \times 10^6$. This is indicative of a delayed separation with increasing Reynolds number, and saturation between $Re = 3 \times 10^6$ and $Re = 4 \times 10^6$.

5.2.2. *Angle of separation*

Figure 11 shows the ratio of axial to transverse velocity at primary separation versus α. High values at low angles of attack indicate that the flow is mainly axial and that the

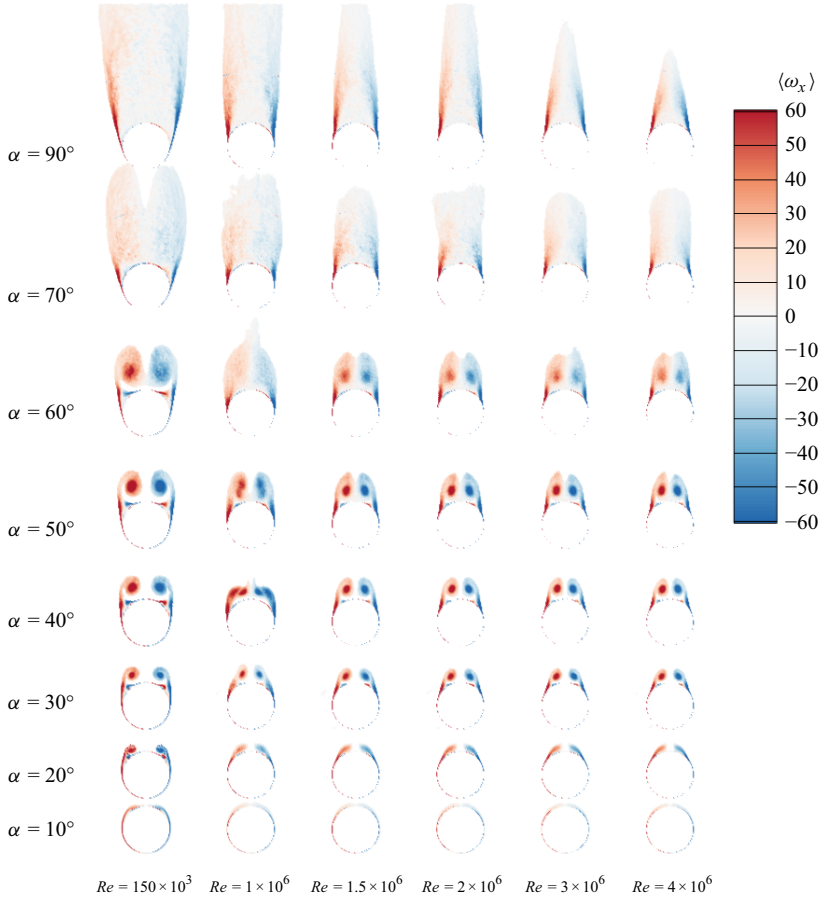

Figure 7. Time-averaged axial vorticity in a transverse slice at $x/L = 0.6$ for all the cases, ordered from left to right by Reynolds number and from bottom to top by angle of attack.

separation is strongly 3-D. The decrease in this ratio with α, to reach 0 at $\alpha = 90°$ is interpreted as the separation becoming closer to a 2-D separation. This decreasing ratio at separation will later be associated with a decreasing swirl number in the vortex. Apart from the 10° case, the Reynolds number has a negligible effect on the value of this ratio.

5.3. *Recirculation*

As discussed in § 5.1, a wide variety of recirculating flows are produced depending on the values of Re, α and the axial location x/L, which can be grouped into three states displayed in figure 12. Figure 12(a) shows the time-averaged stagnation pressure for a 'proto-vortex' state in which the separation is small and confined close to the wall. A weak recirculation is visible, although its centre does not correspond to an extremum of pressure, stagnation pressure, or vorticity. Figure 12(b) shows the Q invariant defined as $Q = (1/2)(\|\Omega\|^2 - \|S\|^2)$ where $\Omega = (1/2)((\partial\bar{u}_i/\partial x_j) + (\partial\bar{u}_j/\partial x_i))$, $S = (1/2)((\partial\bar{u}_i/\partial x_j) - (\partial\bar{u}_j/\partial x_i))$. The positive values indicate the regions dominated by rotational vorticity and can be used to identify coherent vortical structures as proposed by Hunt, Wray & Moin (1988), while the negative values indicate the irrotational straining. Small positive Q values are observed in the proto-vortex case. Figure 12(c) shows a coherent vortex state in which a vortex core is visible, bounded by a closed isoline of

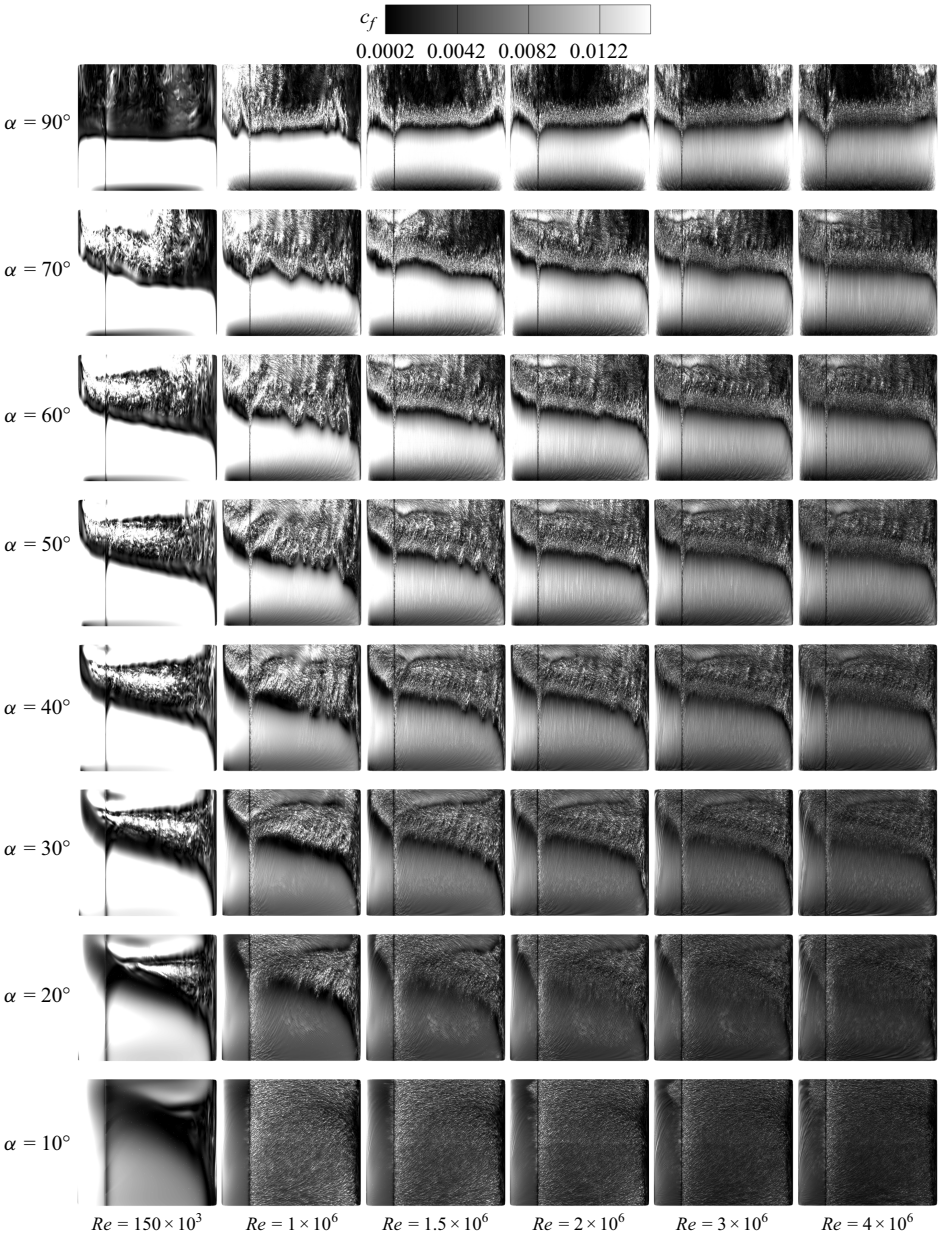

Figure 8. Skin friction coefficient c_f versus x/L and ϕ for $\phi \in [0°, 180°]$, for all the cases, ordered from left to right by Reynolds number and from bottom to top by angle of attack.

stagnation pressure. Similarly to the proto-vortex state, the boundary layer separates on the side of the spheroid, however, the separated shear layer travels farther from the wall and rolls up in a counter-rotating vortex pair. In addition, after attachment on the leeside, the boundary layer separates a second time below the vortex and forms a secondary vortex pair. Large positive Q values are seen in the primary vortex region, small positive values in the secondary vortex on figure 12(*d*), with negative values in the separated shear layer. Figure 12(*e*) shows a recirculating wake without visible coherent vortex. In this state,

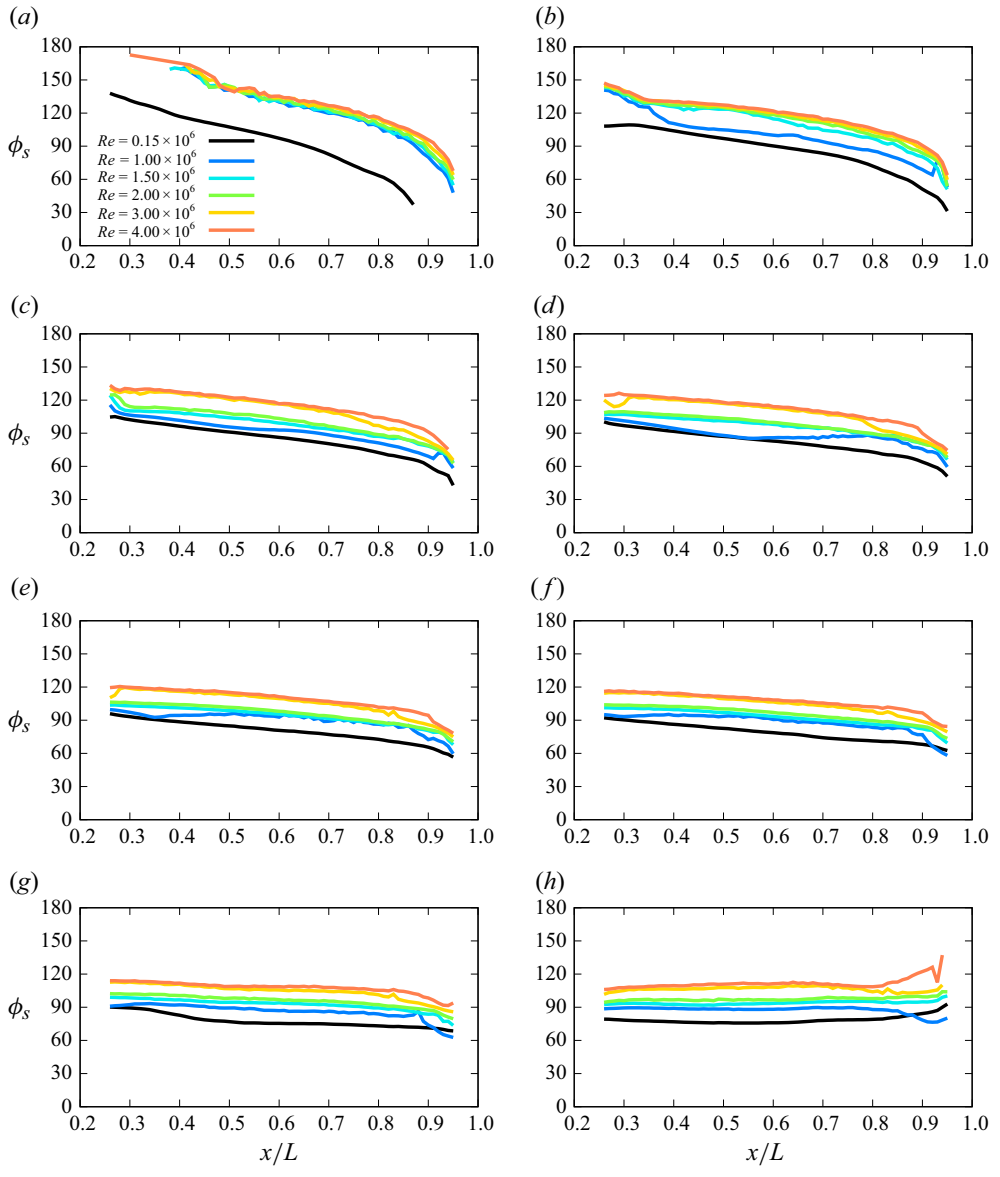

Figure 9. Azimuthal location of primary separation versus x/L, from (*a*) to (*h*): $\alpha = 10°, 20°, 30°, 40°, 50°, 60°, 70°, 90°$.

the shear layer does not reattach and is advected in the free stream direction. The shear layer pair slowly diffuses vorticity with increasing distance from inception. A weak, low-velocity recirculation region is present between the symmetric shear layers. The Q values are close to zero in the recirculation, due to the absence of coherent vortical structure.

In both the proto-vortex and coherent vortex states, the entirety of the separated layer is redirected in the axial direction. In the shedding recirculation state, 2-D streamlines projected in a transverse plane and originating from the separation are unbounded. Thus, part of the flow originating from the separated boundary layer is not carried into the

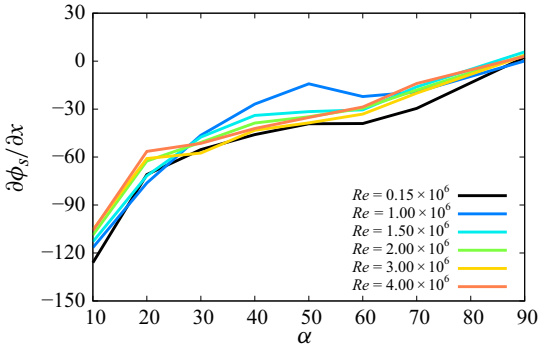

Figure 10. Slope of separation line regression versus angle of attack. Each curve is a different Reynolds number.

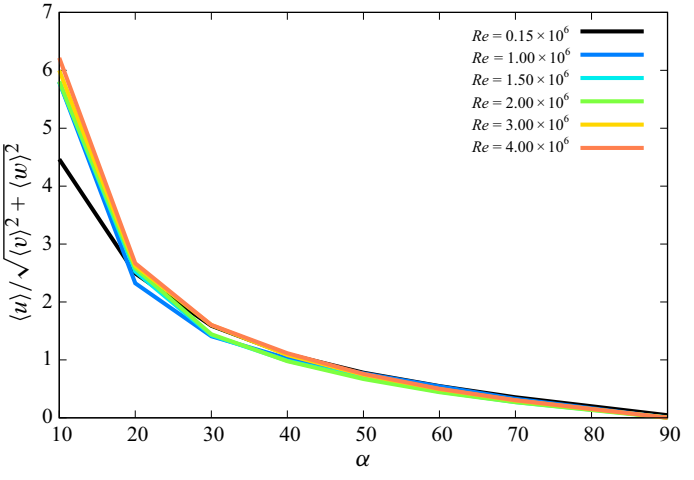

Figure 11. Averaged ratio of axial to transverse velocity at primary separation versus α.

recirculation but is advected along the free stream direction. The following sections describe these three states in more detail.

5.4. *Recirculation in proto-vortex case*

Figure 13 shows the axial velocity, pressure, vorticity magnitude and normalised helicity density at $(x/L, \alpha, Re) = (0.5, 20°, 2 \times 10^6)$, for which a proto-vortex recirculation is formed. The flow can be divided into two layers. The outer layer is formed from the primary separation, moves in the leeward and axial directions, and has a higher vorticity. The inner layer is under the outer layer and travels in the windward direction. In contrast to a coherent vortex, where the transverse velocity is zero at a single point, in the proto-vortex case, the transverse velocity is zero along a boundary between the two layers. The helicity density represents the relative alignment of the velocity with the vorticity: it is zero for a 2-D recirculation and non-zero for a 3-D recirculation. In this case, the helicity density shows the two-layer structure particularly well. The magnitude of the helicity density is smaller at separation and in the outer layer; it is nearly unity in the recirculation region. This indicates that the vorticity is closely aligned with the direction of the streamlines. No localised minimum pressure or vorticity maximum is visible along the boundary. Instead, since the fluid travels in the leeward direction in the outer layer, in the windward direction

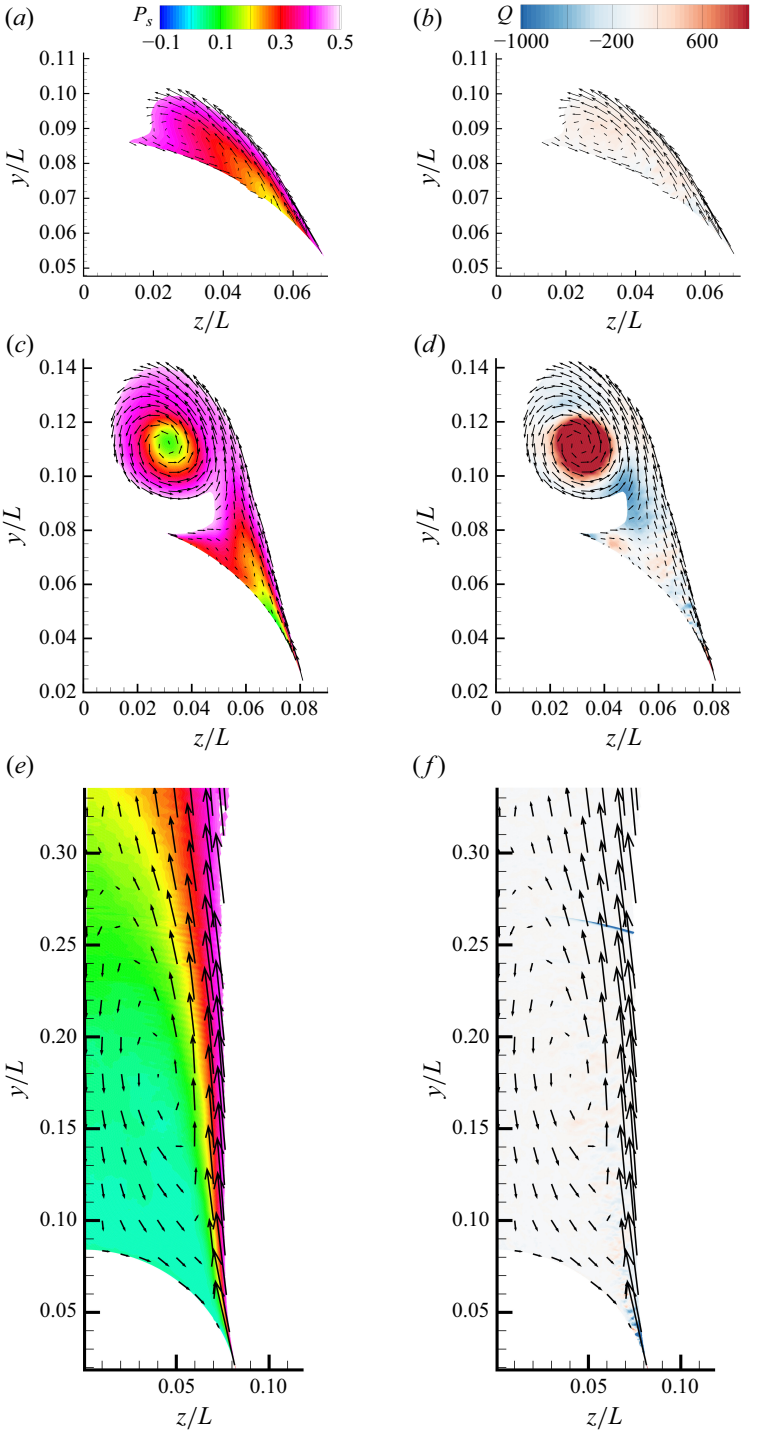

Figure 12. (*a*,*c*,*e*) Time-averaged stagnation pressure and (*b*,*d*,*f*) time-averaged Q invariant in a transverse slice at (*a*) and (*b*): $(x/L, \alpha, Re) = (0.5, 20°, 2 \times 10^6)$, showing the proto-vortex; (*c*) and (*d*) $(x/L, \alpha, Re) = (0.5, 40°, 2 \times 10^6)$, showing the 3-D coherent vortex; (*e*) and (*f*): $(x/L, \alpha, Re) = (0.5, 90°, 2 \times 10^6)$, showing the recirculating wake. A threshold based on $0.49P_s^\infty$ was used as detailed in § 3.5. The length and direction of the arrows are representative of the transverse velocity.

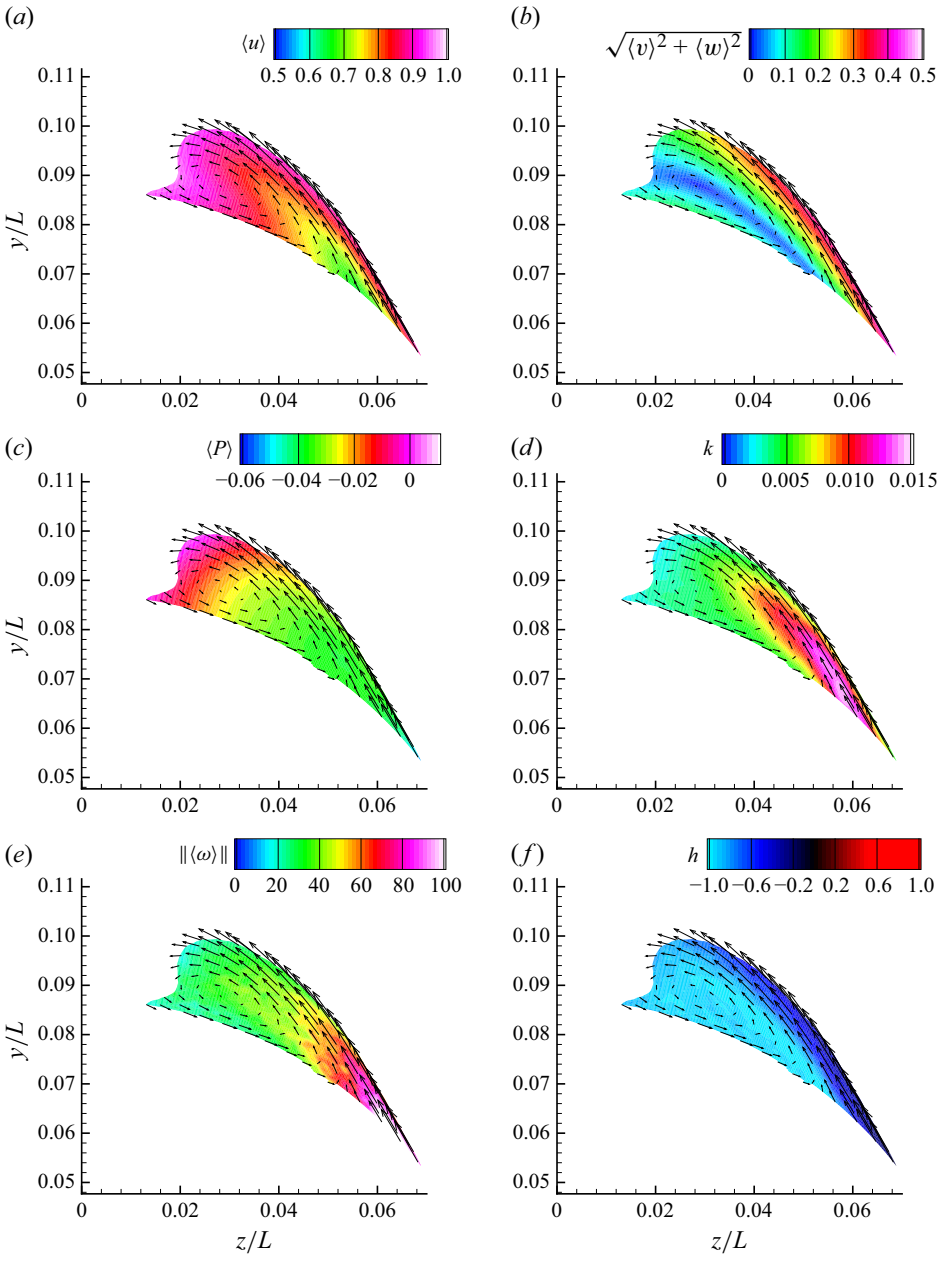

Figure 13. Time-averaged (*a*) axial velocity, (*b*) transverse velocity, (*c*) pressure, (*d*) TKE, (*e*) vorticity magnitude and (*f*) normalised helicity density in a transverse slice at $(x/L, \alpha, Re) = (0.5, 20^\circ, 2 \times 10^6)$, showing the proto-vortex. The length and direction of the arrows are representative of the transverse velocity.

in the inner layer, and the pressure increases azimuthally, an adverse pressure gradient is visible in the outer layer and a favourable pressure gradient is observed in the inner layer.

5.5. *Recirculation in 3-D vortex case*

Figure 14 shows time-averaged stagnation pressure for $(x/L, \alpha, Re) = (0.5, 40^\circ, 2 \times 10^6)$, where the recirculation forms a coherent 3-D vortex. After the primary

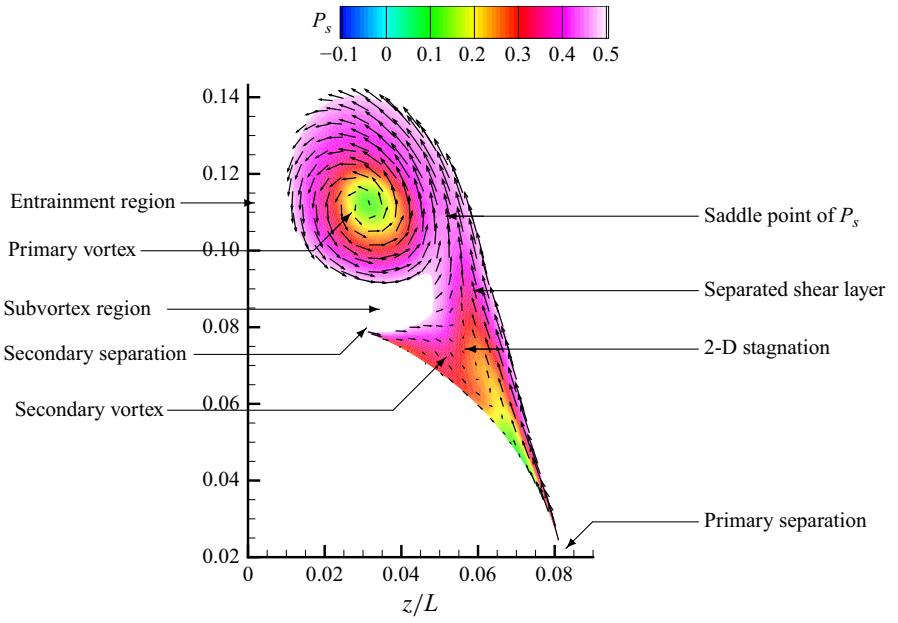

Figure 14. Time-averaged stagnation pressure in a transverse slice at $x/L = 0.7$ for $\alpha = 40°$, $Re = 2 \times 10^6$, showing the coherent 3-D vortex (same view as figure 12*c*, enlarged and with additional annotations). Only the flow where $P_s \leqslant 0.49 P_s^\infty$ is shown. The primary and secondary separations are located as regions of azimuthal change of helicity density. The entrainment region is defined as the area between the primary vortices where $P_s > 0.49 P_s^\infty$. The subvortex region is defined as the area below the primary vortex where $P_s > 0.49 P_s^\infty$. The 2-D stagnation points are points where $\langle v \rangle^2 + \langle w \rangle^2 = 0$. The length and direction of the arrows are representative of the transverse velocity.

separation, the separated boundary layer is convected along the y-direction, where it rolls up into a distinct vortical structure. This vortex entrains flow from the free stream and induces a secondary separation that leads to a secondary vortex rotating in the opposite direction. The following subsections describe each area of the 3-D vortex flow in more detail.

5.5.1. *Separation sheet*

Downstream of the primary separation, the separated shear layer travels tangentially to the wall, with an axial component inversely proportional to the incidence. Figure 15 shows the axial velocity $\langle u \rangle$, transverse velocity, pressure, TKE, vorticity magnitude and normalised helicity density for $(x/L, \alpha, Re) = (0.5, 40°, 4 \times 10^6)$. The shear layer is composed of two sublayers similar to the proto-vortex state: the inner sublayer has low transverse velocity, high axial velocity, while the outer sublayer has high transverse velocity, low axial velocity. The inner layer also has low vorticity, suggesting that the fluid originates from the free stream entrained between the primary vortex pair. The outer sublayer has high vorticity and high TKE. This is related to the large wall pressure and velocity fluctuations that Goody, Simpson & Engel (1998) observed close to separation and into the separation layer, respectively. In addition, the separated shear layer is a pressure maximum and has a helicity density close to unity, which indicates that the axis of vorticity is closely aligned with the streamlines. This observation is consistent with a vortex comprised of small helical vortices as seen in DNS in the laminar *Re* regime (Jiang *et al.* 2016; Strandenes

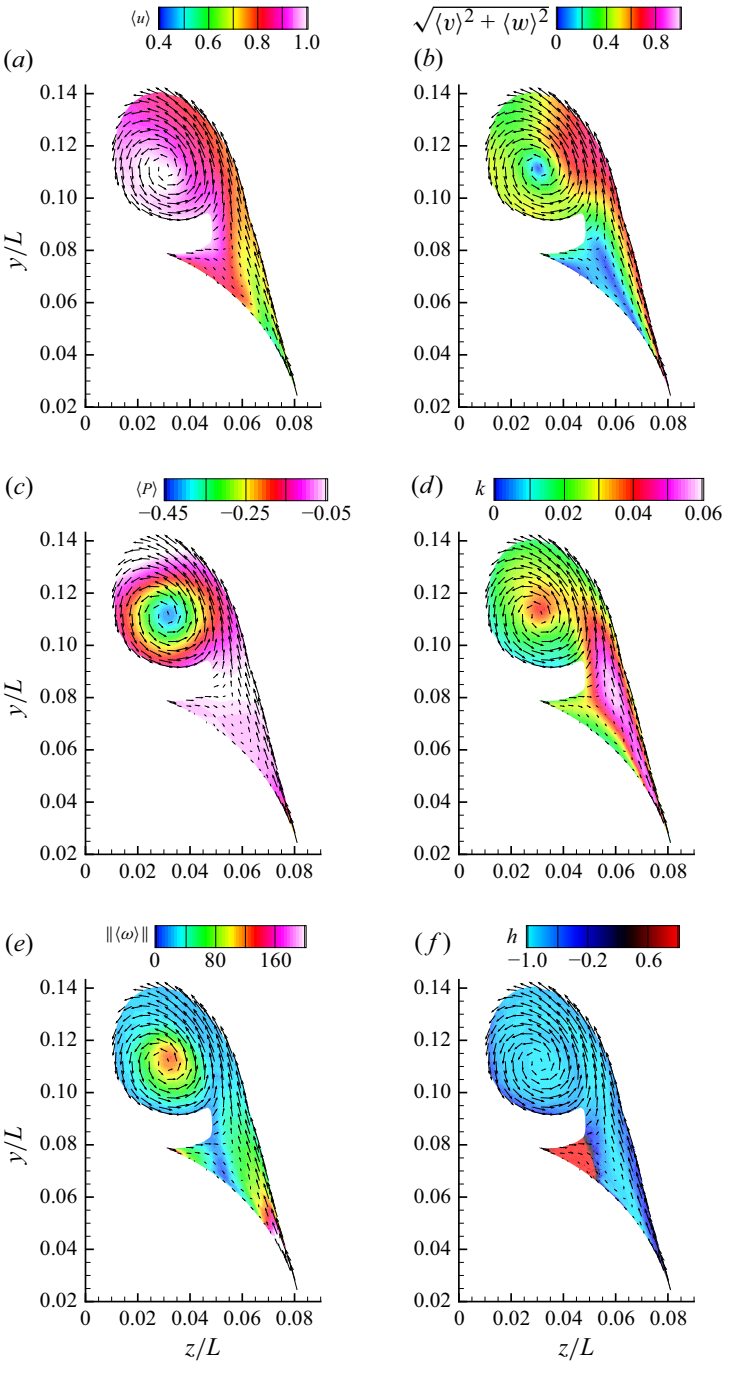

Figure 15. Time-averaged (*a*) axial velocity, (*b*) transverse velocity, (*c*) pressure, (*d*) TKE, (*e*) vorticity magnitude and (*f*) normalised helicity density in a transverse slice at $x/L = 0.7$ for $\alpha = 40°$, $Re = 2 \times 10^6$.

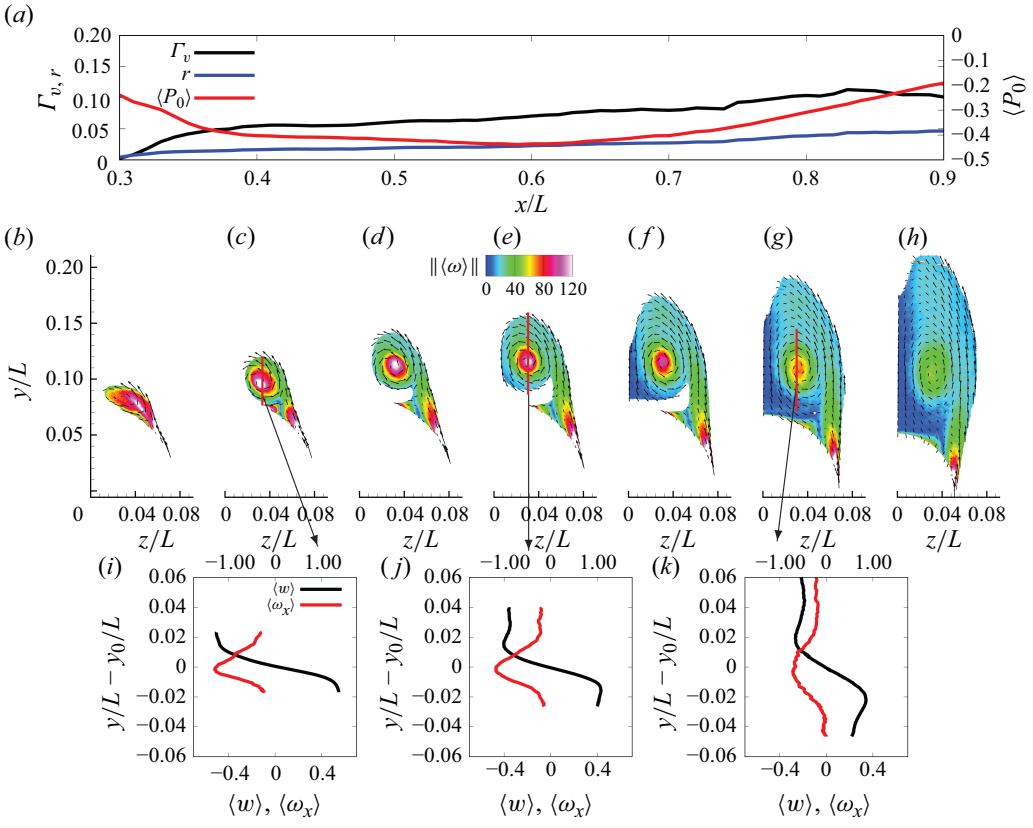

Figure 16. Evolution of the recirculation for $\alpha = 40°$, $Re = 2M$, $x/L \in [0.3, 0.9]$: (*a*) vortex circulation Γ_v, vortex radius r and vortex centre pressure $\langle P_0 \rangle$ versus x/L; (*b*) through (*h*) time-averaged vorticity in a transverse slice at $x/L = 0.3, 0.4, 0.5, 0.6, 0.7, 0.8, 0.9$; (*i*, *j*) and (*k*) time-averaged spanwise velocity (black curve) and time-averaged axial vorticity (red curve) along a vertical profile centred on the vortex at $y = y_0$, at $x/L = 0.4, 0.6, 0.8$.

et al. 2019). This structure consisting of small vortices in the separation layer, helically wrapped to form a coherent vortex, is not unique to the spheroid and has been observed in the flow over a ducted propeller (Leasca *et al.* 2025). The higher TKE in this location was also observed by Chesnakas & Simpson (1996). The shear layer is then accelerated outside the vortex by a favourable pressure gradient, correlated with a decrease in vorticity and TKE. The shear layer then attaches to the primary vortex at a point that will be referred to as the saddle point. This terminology is used because $(\partial P_s/\partial\theta) = 0$, $(\partial P_s/\partial r) = 0$, $(\partial^2 P_s/\partial r^2) \times (\partial^2 P_s/\partial\theta^2) < 0$, where (r, θ) are the cylindrical coordinates with respect to the centre of the vortex. This point lies on the boundary of the vortex and is used to assess the highest value of stagnation pressure inside it.

5.5.2. *Primary vortex*

Figure 15 shows that the primary vortex itself can be divided into two regions. The first outer region originates from the roll-up of the separated shear layer as previously discussed. The inner region, or vortex core, is nearly axisymmetric about the vortex centre, has high vorticity, high TKE, low pressure and normalised helicity density close to one. Unity of the normalised helicity density means that the orientation of the vorticity vector is closely aligned with the orientation of the velocity vector.

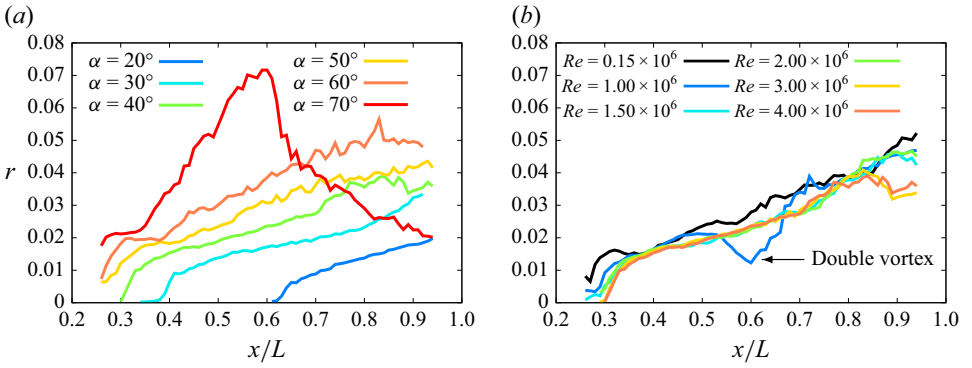

Figure 17. Primary vortex radius r versus x/L for $\alpha \in [20°, 70°]$, $Re = 4 \times 10^6$ (a) and for $\alpha = 40°$, $Re \in [0.15 \times 10^6, 4 \times 10^6]$ (b).

The evolution of the recirculation from $x/L \in [0.3, 0.9]$, $\alpha = 40°$ and $Re = 2M$ is shown in figure 16. The vortex grows linearly with the axial coordinate, both in mean radius and circulation, from $x \approx 0.35L$ to $\approx 0.85L$. The axial pressure gradient is favourable from $x = 0.3L$ to $\approx 0.6L$ and adverse from $\approx 0.6L$ to $x = 0.9L$. The tangential velocity in the vortex increases linearly with r until it peaks and decreases. The axial vorticity profile follows a bell curve centred on the vortex. Both tangential velocity and axial vorticity have higher peaks and higher slopes at $x = 0.4L$ compared with $x = 0.6L$ and $x = 0.8L$. Both profiles also spread with x as the vortex grows. The remainder of this paragraph will show that similar behaviour is observed for the other cases, albeit at different rates.

Figure 17 shows the radius of the primary vortex along the spheroid for $\alpha \in [20°, 70°]$, $Re = 4 \times 10^6$ and for $\alpha = 40°$, $Re \in [0.15 \times 10^6, 4 \times 10^6]$. Three regions are observed.

(i) Early in the vortex formation, the radius increases linearly with a large slope ($> 0.2r/(x/L)$) for a short distance ($\approx 0.1x/L$).
(ii) The large increase is followed by a slower increase ($\approx 0.04r/(x/L)$) until the tail of the spheroid for $\alpha \leq 30°$ and until $x/L \approx 0.6$ at $\alpha = 50°$ and $x/L \approx 0.4$ for 70°. The angle of attack does not have a strong effect on this slope.
(iii) For $\alpha = 70°$, a rapid linear increase is followed by a decrease in radius at high Re.

Note that the case $(\alpha, Re) = (40°, 1 \times 10^6)$ shows a deviation with the linear increase, which is due to the merger of two corotating primary vortices. This merger is visible in figures 18(a) and 19, representing the time-averaged stagnation pressure in the lee of the spheroid. For comparison, a more commonly observed single vortex formation is provided in figure 18(b), obtained for $(\alpha, Re) = (40°, 4 \times 10^6)$. This also shows the linear increase of the vortex radius and the near-collinearity of the axis of the vortex with the axis of the spheroid, both of which have been previously observed in figure 17 and confirmed in figure 20 showing a linear slope of $\log(r)$ versus $\log(x)$.

The evolution of the recirculation in figure 21 follows a similar evolution as the radius, except the increase is mostly linear for $\alpha \leqslant 30°$ and a clearer positive correlation between the slope and the angle of attack. The circulation increases monotonically for $\alpha \leqslant 30°$. For $\alpha > 30°$, the circulation increases, peaks and decreases until the tail of the spheroid. This peak occurs increasingly early with increasing incidence, such that at $\alpha = 70°$, the circulation is highest at $x \approx 0.4L$ and decreases from that point until the tail of the spheroid. These three-part curves correspond to the three phases of the vortex mentioned in the discussion of figure 17: inception, development and decay. The slope of increase in

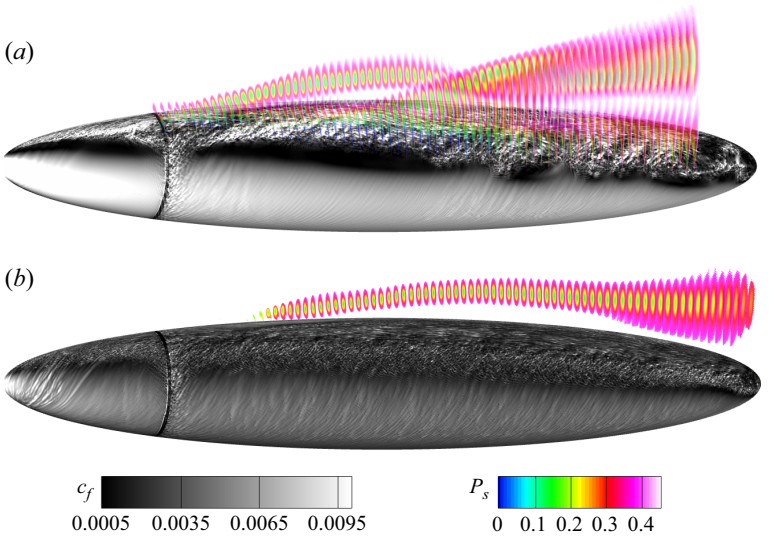

Figure 18. Visualization of the spheroid at (*a*) $\alpha = 40°$ and $Re = 1 \times 10^6$; (*b*) $\alpha = 40°$ and $Re = 4 \times 10^6$. The wall of the spheroid is shaded by instantaneous skin friction coefficient; one half of the flow ($\phi \in [0°, 180°]$) is shown in transverse slices spaced by $\Delta x = 0.01$ and shaded by time-averaged stagnation pressure.

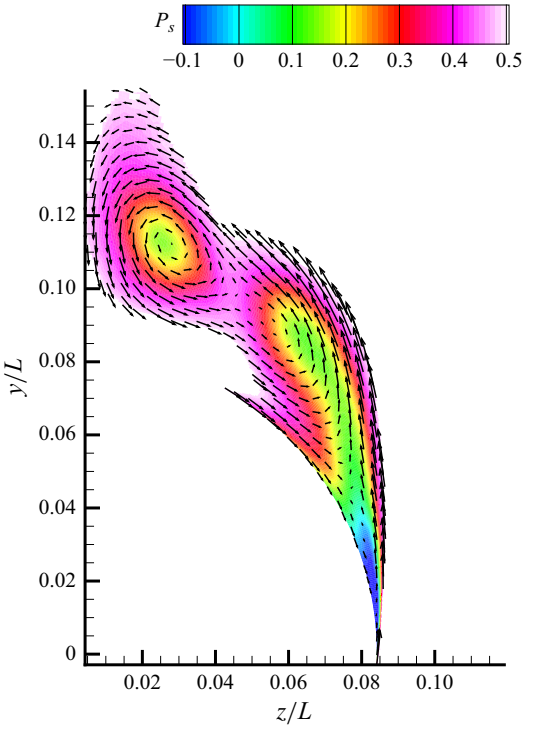

Figure 19. Time-averaged stagnation pressure in a transverse plane at $\alpha = 40°$, $Re = 1 \times 10^6$, $x/L = 0.55$ showing the merger of two corotating primary vortices.

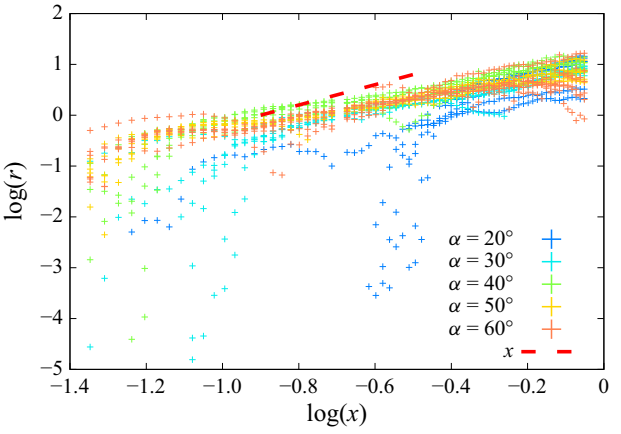

Figure 20. Logarithm of the primary vortex radius versus $\log(x)$ for $\alpha \in [20°, 60°]$.

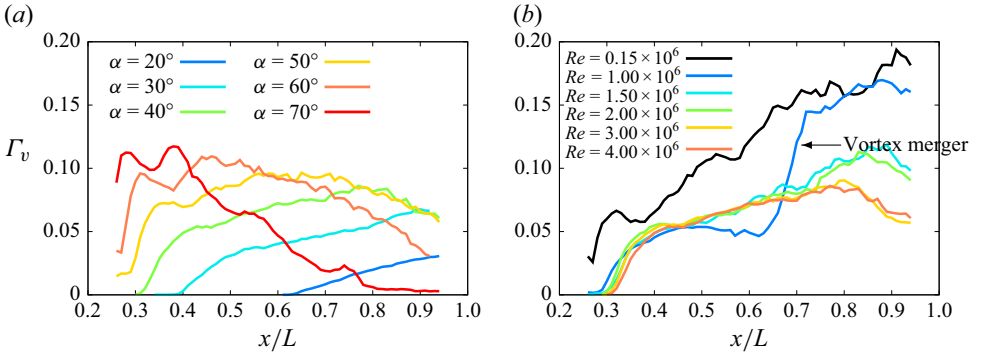

Figure 21. Primary vortex circulation versus x/L for $\alpha \in [20°, 70°]$, $Re = 4 \times 10^6$ (*a*) and for $\alpha = 40°$, $Re \in [0.15 \times 10^6, 4 \times 10^6]$ (*b*).

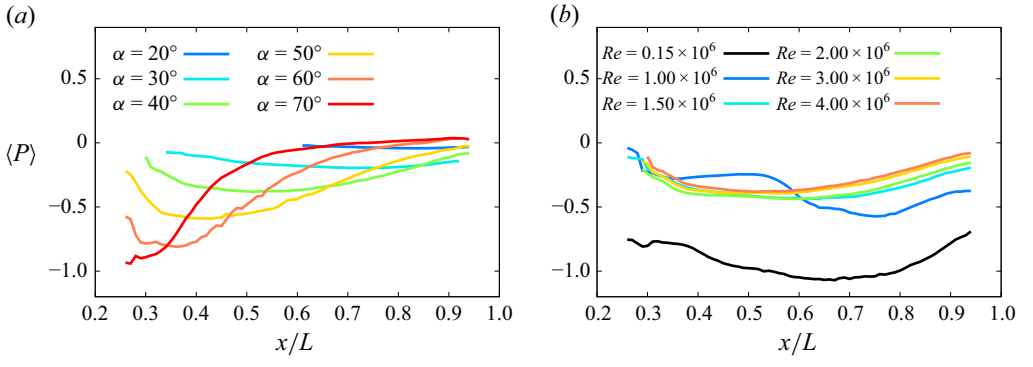

Figure 22. Pressure at the centre of the primary vortex versus x/L for $\alpha \in [20°, 70°]$, $Re = 4 \times 10^6$ (*a*) and for $\alpha = 40°$, $Re \in [0.15 \times 10^6, 4 \times 10^6]$ (*b*).

circulation is weakly correlated with α or Re, although the slope of decay is higher for higher incidences. For all angles, the $Re = 0.15 \times 10^6$ cases are distinctly larger than the higher Reynolds numbers, although the behaviour is similar.

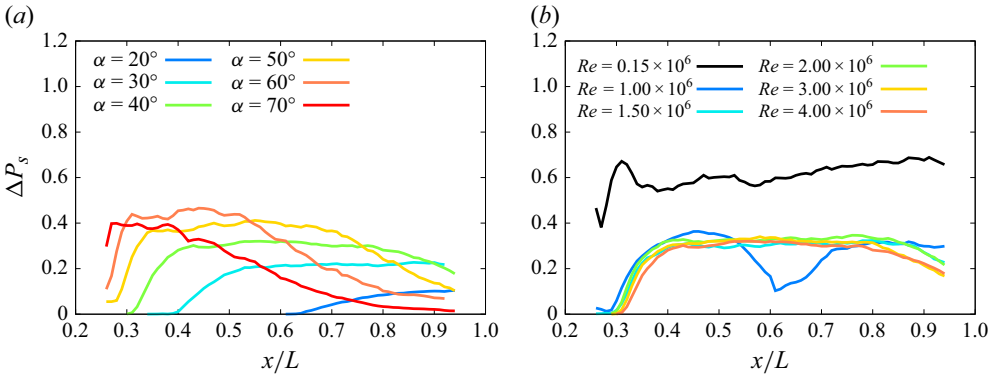

Figure 23. Stagnation pressure differential in the primary vortex versus x/L for $\alpha \in [20°, 70°]$, $Re = 4 \times 10^6$ (*a*) and for $\alpha = 40°$, $Re \in [0.15 \times 10^6, 4 \times 10^6]$ (*b*).

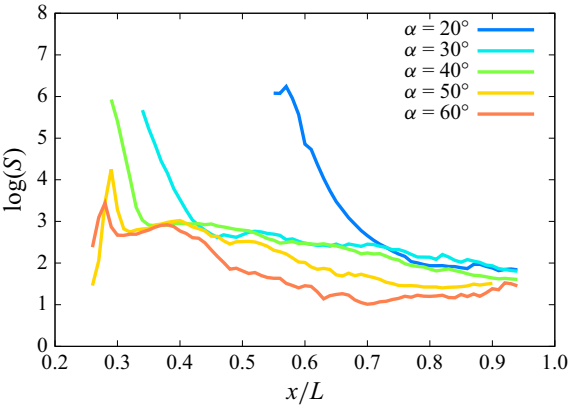

Figure 24. Swirl number versus x for $\alpha \in [20°, 60°]$, $Re = 2 \times 10^6$.

Figures 22 and 23 show the pressure in the centre of the vortex and the stagnation pressure differential $\Delta P_s = P_s^{saddle} - P_s^0$ where P_s^{saddle} is the stagnation pressure at the saddle point and P_s^0 is the stagnation pressure at the centre. Both P and ΔP_s can be split into three regions corresponding to the three stages of the vortex: at the inception of the vortex, the pressure drops and the stagnation pressure differential rises; during the main development, the pressure has small variations and ΔP_s remains remarkably constant; during the decay of the vortex, both the centre pressure and ΔP_s converge to 0.

Figure 24 shows the swirl S in the vortex for $Re = 2 \times 10^6$, $\alpha \in [20°, 60°]$. The swirl number S is defined as the ratio of transverse flux to axial flux (Reynolds 1962). The curves can be decomposed into three successive behaviours.

(i) Fast initial decay at the formation of the vortex (three orders of magnitude in $\Delta x = 0.05L$ at $\alpha = 40°$). The start of the decay occurs closer to the nose for higher values of α. These high swirl values are the consequence of high vorticity and small vortex radius at the inception of the vortex. The maximum values of swirl are overall higher for lower angles of attack.

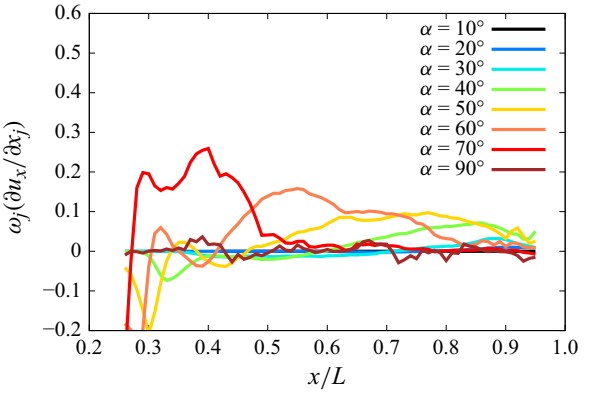

Figure 25. Vortex stretching/tilting $\omega_j(\partial u_x/\partial x_j)$ in the recirculation versus x/L for $Re = 2 \times 10^6$.

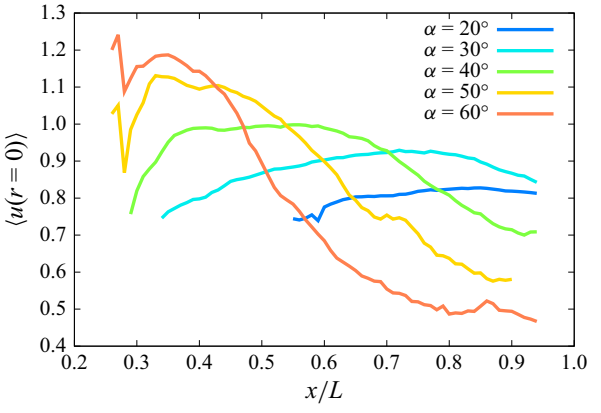

Figure 26. Vortex centre velocity for $\alpha \in [20°, 60°]$ versus x/L for $Re = 2M$.

(ii) Slower quadratic decay $S \propto x^{-2}$ (slightly faster decay for $\alpha \geqslant 50°$), which is related to a faster increase in vortex area ($\sim x^2$) compared with its increase in circulation ($\sim x$).

(iii) For $\alpha \geqslant 50°$: almost constant swirl number $10 < S < 100$ from $x/L \approx 0.75$ to $x/L = 0.95$.

The axial vortex stretching/tilting versus x/L for all angles of incidence and $Re = 2 \times 10^6$ is shown in figure 25. Negative values are interpreted as an axial stretching while positive value are indicative of an axial compression. The recirculation initially goes through a phase of axial stretching, followed by compression. The transition from stretching to compression occurs increasingly earlier with increasing angle of attack.

Figure 26 shows the axial velocity in the centre of the vortex for $\alpha \in [20°, 60°]$, $Re = 2 \times 10^6$. Increasing values are representative of accelerating axial flow and stretching of the vortex, while decreasing values are indicative of decelerating axial flow. The vortex is initially stretched, followed by a compression phase. The phases of stretching and compression are consistent with the favourable and adverse pressure gradient observed in figure 16.

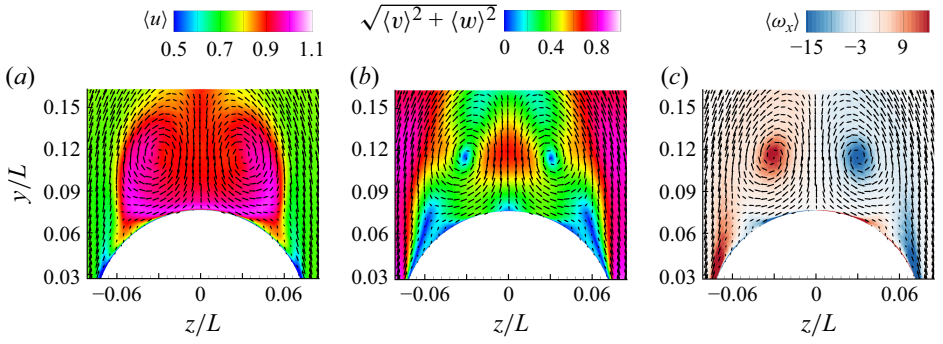

Figure 27. Time-averaged (*a*) axial velocity, (*b*) transverse velocity and (*c*) axial vorticity in the entrainment zone in a transverse slice at $x/L = 0.7$ for $\alpha = 40°$, $Re = 2 \times 10^6$.

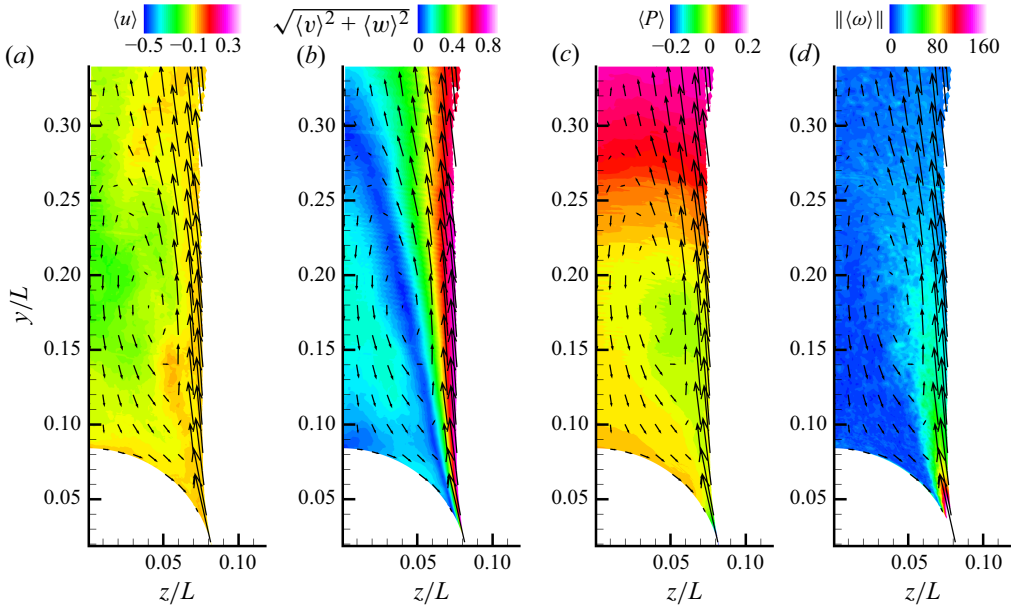

Figure 28. Time-averaged (*a*) axial velocity, (*b*) transverse velocity magnitude, (*c*) pressure and (*d*) vorticity magnitude for $(x/L, \alpha, Re) = (0.5, 90°, 2 \times 10^6)$.

5.5.3. *Entrainment zone and subvortex region*

Figure 27 shows the time-averaged axial velocity component, transverse velocity and axial vorticity in and around the entrainment region. After the previously discussed deceleration on the outer side of the primary vortex, the flow is accelerated in the transverse direction to reach a maximum between the vortex pair on the leeside meridian plane. At this location, the velocity vector is aligned with the negative y direction. From then on, the axial velocity increases to reach a maximum close to the wall on the same vertical plane. The flow is redirected on each side of the meridian plane to pass between the primary vortex and the secondary vortex before intersecting the separated shear layer at $z = \pm 0.05L$. This entrainment is related to the downwash created in the lee and wake of profiled geometries. Close to the wall, a boundary layer forms starting from $\phi = 180°$ and travels in the opposite azimuthal direction as the primary boundary layer. This boundary layer separates below the primary vortex and forms a secondary vortex pair, visible as a region of opposite axial

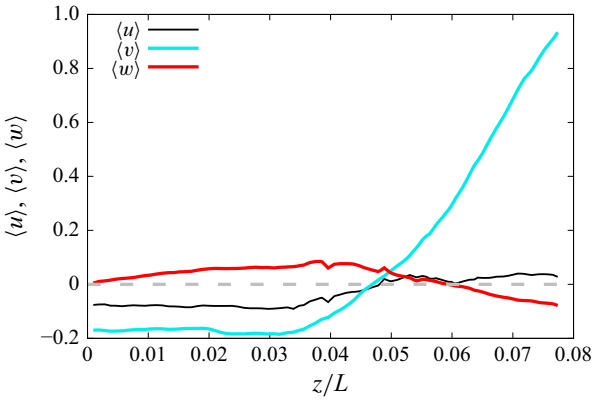

Figure 29. Three components of time-averaged velocity in the body frame of reference along the span direction z for $(x/L, \alpha, Re) = (0.5, 90°, 2 \times 10^6)$ at $y = 0.15L$ from the axis of the spheroid. The zero-velocity line is drawn in grey for ease of reading.

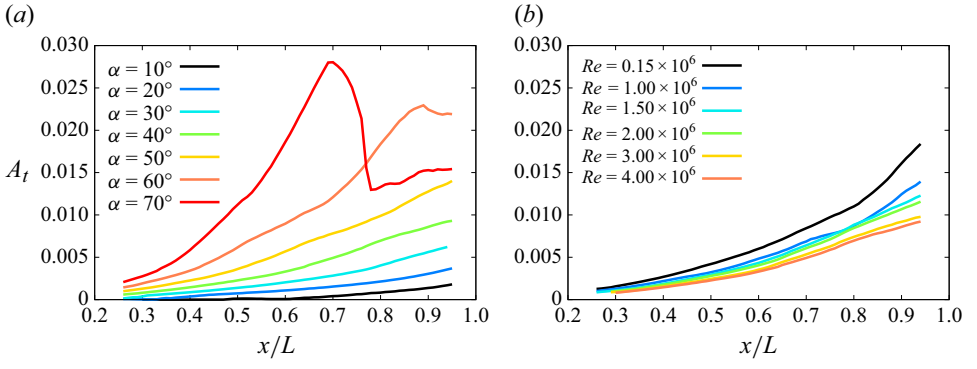

Figure 30. Total recirculation area versus x/L for $\alpha \in [20°, 70°]$, $Re = 4 \times 10^6$ (a) and for $\alpha = 40°$, $Re \in [0.15 \times 10^6, 4 \times 10^6]$ (b).

vorticity compared with the primary vortex of the corresponding side. Four 2-D stagnation points are observed in this flow: one for $\phi = 180°$, above the primary vortex pair where the separated shear layers intersect; one at $\phi = 180°$, where the entrainment sheet intersects the wall; one on each side where the entrainment flow intersects the separated shear layers.

5.6. *Recirculating wake*

Figure 28 shows axial velocity, transverse velocity, pressure and enstrophy in one half of the recirculating wake at $(x/L, \alpha, Re) = (0.5, 90°, 2 \times 10^6)$. Downstream of separation, the separated shear layer does not form a coherent vortex. Instead, the projections of the streamlines in the transverse plane from the separation are unbounded. The pair of separated layers meet at a 2-D stagnation point on the lee meridian plane. The distance between this 2-D stagnation point and the wall is called the local separation length L_s and is studied in more detail in § 5.7. The vorticity carried by the shear layer slowly diffuses in the streamwise direction. The symmetric pair of shear layers forms a cavity where the pressure, stagnation pressure and vorticity have small gradients and where the fluid slowly recirculates back towards the leeside wall of the spheroid.

Figure 29 shows the components of velocity on a line that runs in the z direction, at $y = 0.15L$. The vertical velocity $\langle v \rangle$ is larger than the other two components. Two regions

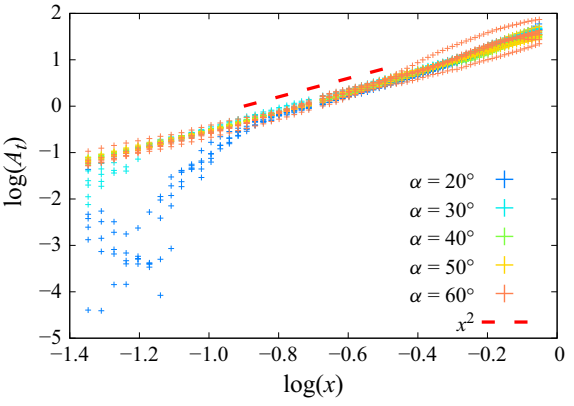

Figure 31. Logarithm of the recirculation area versus $\log(x)$ for $\alpha \in [20°, 60°]$.

are visible: for $z < 0.04L$, the axial and vertical components are negative, while the spanwise component is positive. All three components are almost constant in this region. The spanwise component is 0 at $z = 0$ by symmetry and increases slightly until $z = 0.04L$. This region corresponds to the cavity, as observed in figure 28. For $z > 0.04L$, all three components switch sign, the vertical velocity increases the fastest to match the free stream value. This transitional region corresponds to the separated shear layer.

5.7. *Evolution of recirculation area with axial location*

A 'total recirculation area' was previously defined in § 3 as the region downstream of separation where $P_s < 0.49 P_s^\infty$. This area is used to study the recirculation independent of its state. Figure 30(a) represents the area of recirculation A_t versus the axial distance for $Re = 4 \times 10^6$ and $\alpha \in [10°, 70°]$, figure 30(b) shows A_t versus x/L for all the Reynolds numbers and $\alpha = 40°$. For $\alpha \leqslant 50°$, the area increases monotonically. The slope of the curves increases with decreasing Reynolds numbers. For $\alpha \geqslant 70°$, the area increases until $x/L \approx 0.7$ for $\alpha = 70°$, at which point the area decreases. This decrease corresponds to a state change in the recirculation topology, dividing a regime in which the primary vortex is coherent from a regime in which the recirculation is decoherent. The slope of the A_t versus x curve is increasingly steeper with increasing angle of attack. This is representative of the faster axial growth of the recirculation area at higher angles of attack and mirrors the linear rise of the radius of the vortex (see figure 17). A smaller albeit noticeable correlation is also observed between the slope of the curve and Re, with lower Reynolds numbers having higher slopes. This indicates an increased growth of the recirculation area with decreasing Re. This is consistent with the qualitative observation made in figure 7.

Figure 31 shows the log of the total area versus the log of the axial coordinate for $\alpha \in [20°, 60°]$. The slope of the curve is close to 2, showing quadratic scaling of A_t with x, for a large portion of the cases. For $\alpha = 20°$ and $\alpha = 30°$, A_t initially rises faster than x^2 when the area is small, but then converges to a slope of x^2. In addition, the area of the recirculation only follows a quadratic curve when the recirculation is coherent. When a recirculating wake is formed, the vertical extent of the area with non-zero vorticity may become unbounded. In that case A_t becomes undefined.

Figure 32 shows the total circulation versus the axial direction. Unlike the area itself, which increased quadratically, the leeside circulation increases more slowly. This linear increase is related to an almost constant vorticity flow rate at separation. Linear increase in circulation coupled with quadratic increase in area translates into a lower average circulation with increasing x. It also suggests axial compression of the flow in the axial

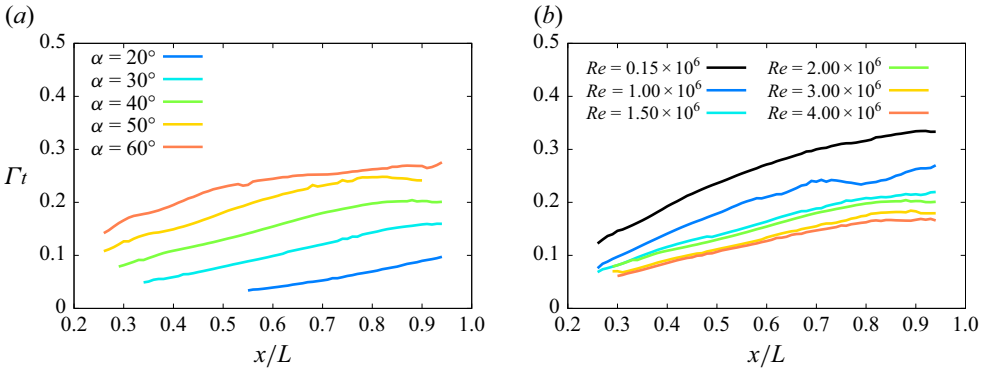

Figure 32. Recirculation circulation versus x/L for (*a*) $\alpha \in [20°, 60°]$, $Re = 4 \times 10^6$; (*b*) $\alpha = 40°$, $Re \in [0.15 \times 10^6, 4 \times 10^6]$.

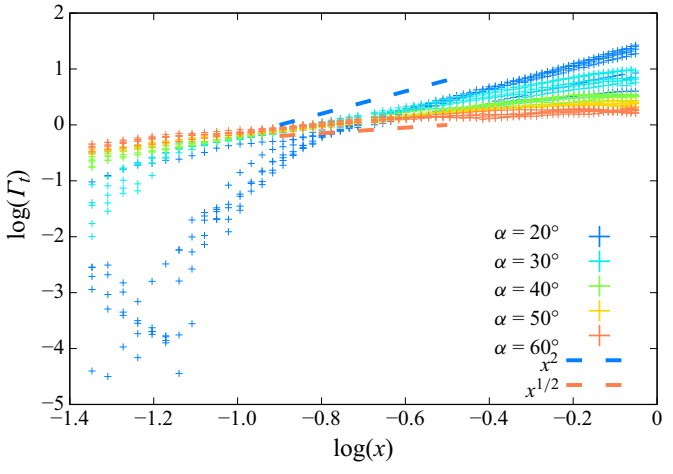

Figure 33. Logarithm of the total circulation versus $\log(x)$ for $\alpha \in [20°, 60°]$.

direction, and is consistent with the decrease of swirl observed in figure 24 and mirrors the compression observed on the vortex.

Figure 33 shows the logarithm of total circulation versus the logarithm of x. Similar to the total area (figure 31), the total circulation follows a power law where all the cases with the same incidence have the same slope regardless of Re, however, that slope changes with α. The circulation in the cases with the lowest incidences follows a quadratic law, while the circulation scales with $x^{1/2}$ at $\alpha = 60°$.

Figure 34 shows a schematic of the control volume surrounding the recirculation volume, which is used to better understand these scalings. The conservation of mass in this control volume can be written as

$$\int_{\mathcal{S}_i} \boldsymbol{u} \cdot \hat{n} \, \mathrm{d}S_i + \int_{\mathcal{S}_{Ps}} \boldsymbol{u} \cdot \hat{n} \, \mathrm{d}S_{Ps} + \int_{A_t(x)} \boldsymbol{u} \cdot \hat{n} \, \mathrm{d}y \, \mathrm{d}z + \int_{A_t(x+\Delta x)} \boldsymbol{u} \cdot \hat{n} \, \mathrm{d}y \, \mathrm{d}z = 0. \quad (5.1)$$

In the inviscid limit, $\mathcal{S}_{Ps}$ has constant stagnation pressure and is therefore a material surface (Plasseraud & Mahesh 2024*a*), and the mass flow rate across that surface is zero. Here $\int_{A_t(x)}$ and $\int_{A_t(x+\Delta x)}$ are normal to the axial direction, so $\boldsymbol{u} \cdot \hat{n} = u.\mathcal{S}_i$ is the only

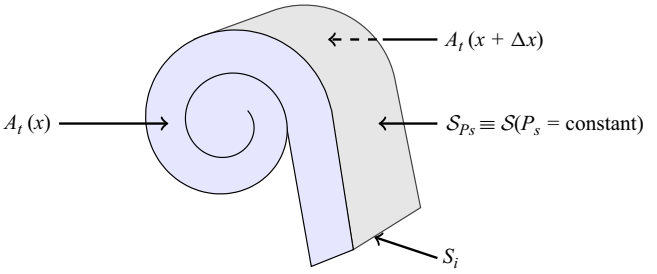

Figure 34. Schematic of the control volume of the recirculation area, bounded by $\mathcal{S}_i$, a surface cutting across the separated shear layer (as seen in figure 14) between x and $x+\Delta x$; $\mathcal{S}(P_s = \text{constant})$, the surface of constant stagnation pressure surrounding recirculation area; $A_t(x)$ and $A_t(x+\Delta x)$, the area of recirculation area at x and $x+\Delta x$, respectively.

surface left to balance the growth of A_t:

$$\int_{\mathcal{S}_i} \boldsymbol{u}\cdot\hat{n}\,\mathrm{d}S_i + \int_{A_t(x)} u\,\mathrm{d}y\,\mathrm{d}z - \int_{A_t(x+\Delta x)} u\,\mathrm{d}y\,\mathrm{d}z = 0. \tag{5.2}$$

We write $\int_{\mathcal{S}_i} \boldsymbol{u}\cdot\hat{n}\mathrm{d}S \equiv \mathcal{I}\Delta x$ where $\mathcal{I}$ is the net mass flow rate added to the recirculation per unit axial length. Note that the inflow may come from the primary separation and the entrainment region,

$$\Leftrightarrow \mathcal{I}\Delta x + \int_{A_t(x)} u\,\mathrm{d}y\,\mathrm{d}z - \int_{A_t(x+\Delta x)} u\,\mathrm{d}y\,\mathrm{d}z = 0, \tag{5.3}$$

$$\Leftrightarrow \frac{\mathrm{d}}{\mathrm{d}x}\left[\int_{A_t} u\,\mathrm{d}y\,\mathrm{d}z\right] = \mathcal{I}. \tag{5.4}$$

This relation can be put into perspective with the linear increase in axial mass flow rate observed in the recirculation area, suggesting that the mass flow rate at separation is independent of x. Although the axial mass flow rate is linear, the area of recirculation is quadratic. This means that the mean axial velocity decreases and that the recirculation is squeezed in the axial direction. This is consistent with the decrease in swirl in the vortex (figure 24).

The quadratic increase for the area can also be understood by analogy to the cavity formed by a cylinder at $\alpha = 90°$ as described by Roshko (1993) and Williamson (1996). In that case, the cavity, also called the 'mean recirculation region', extends to a point of maximal transverse fluctuation along the leeward meridian plane. The distance between that point and the wall is called the formation length and is similar to the previously defined local separation length L_s. A Riabouchinsky model can be created for such a cavity as shown in figure 35, in which the viscous and turbulent stresses of the shear layers τ_s balance the linear pressure suction at the wall $f_y(x)$ (Riabouchinsky 1921),

$$\int_{\phi_s}^{\pi/2} p\,\mathrm{d}\phi \equiv f_y(x) = \int_{\mathcal{S}} \tau_s \propto L_s\tau_s, \tag{5.5}$$

where $\mathcal{S}$ is the boundary of the cavity. This expression relates the force applied to the cavity and the separation length. In the case of the spheroid, the separated shear layer is tangential to the spheroid at separation ϕ_s. If $\phi_s > 90°$, the boundary of the cavity is angled towards the meridian plane and the cavity width decreases with the distance from the wall until $y = y_s = L_s + y_w$ where y_w is the distance from the centreline of the spheroid to the wall. El Khoury, Andersson & Pettersen (2012) measured this local separation length using

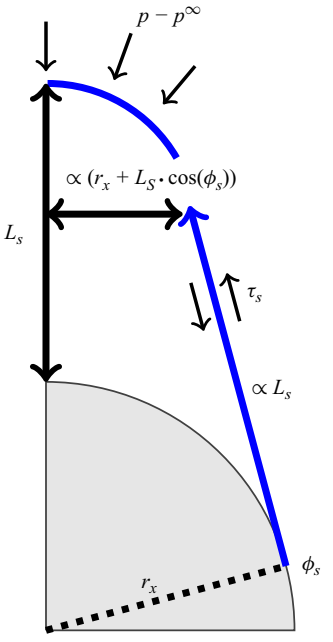

Figure 35. Schematic of the Riabouchinsky model for the prolate spheroid recirculation area.

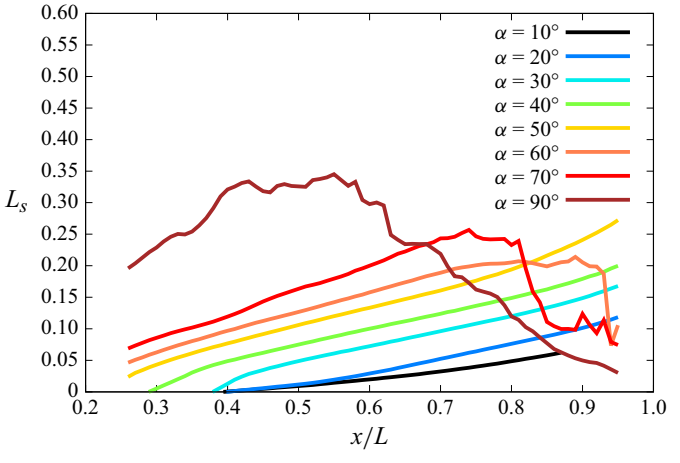

Figure 36. Local separation length L_s versus x/L.

DNS of the spheroid at low Reynolds number for $\alpha = 90°$ and observed that L_s increases linearly with the distance from the tips in the steady case and is maximum at $x/L = 0.5$. At higher *Re*, they also observed that L_s flattens in the midsection of the spheroid.

Figure 36 shows the local separation length for all the cases considered. For $\alpha < 60°$, L_s increases linearly with x. For $\alpha = 60°$ and $\alpha = 70°$, L_s increases linearly, stagnates and decreases more rapidly. At $\alpha = 90°$, L_s has a trapezoidal shape similar to the description of El Khoury *et al.* (2012). The linear increase of L_s is related to the decrease in the azimuth of separation observed in figure 11, which opens the angle of the separated shear layer. In turn, the opening of the angle of the separated shear layer increases the width of the recirculation, which can be scaled as $r_x + L_s\cos(\phi_s)$, where r_x is the radius of the

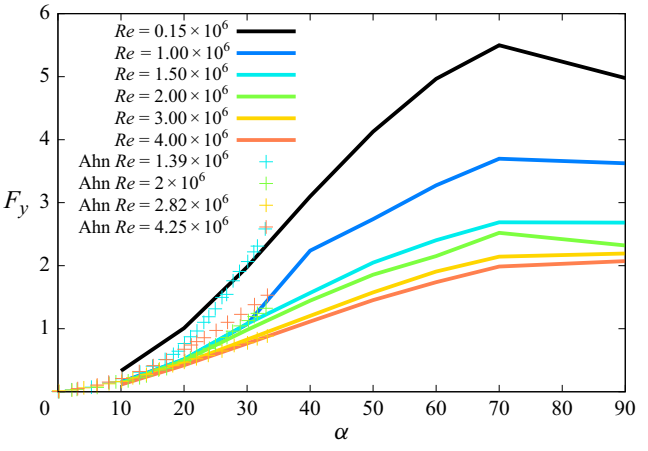

Figure 37. Normal force coefficient F_y versus angle of attack α for all six Reynolds numbers. The dotted lines are experimental results from Ahn (1992).

spheroid for any given x. Thus, the area of recirculation can be scaled as $A_t \propto L_s \times (r_x + L_s \cos(\phi_s))$. If $\phi_s \approx \pi/2$, $A_t \propto L_s \times (r_x + L_s(\pi/2 - \phi_s))$. Since $L_s \propto x$, $A_t \propto x^2$ in the leading order, as previously observed. This plateau observed at $\alpha = 90°$ is understood to be similar to the previously commented vortex burst.

5.8. *Loads*

5.8.1. *Effect of Re and α on the loads*

Figure 37 shows the normal force versus the angle of attack. The force increases from $\alpha = 10°$ to $70°$ for all Reynolds numbers and is constant or decreasing for $\alpha > 70°$. The force is larger at lower Reynolds numbers, particularly for the two lowest ones and for $\alpha > 40°$. The effect of Reynolds number is smaller at the higher Reynolds numbers ($Re \geqslant 1.5 \times 10^6$). The rise in normal force for $\alpha < 70°$ and decrease for $\alpha > 70°$ correlates with the observed steepening of the slope of the vortex circulation versus x, as α increases. The plateau of the force between $\alpha = 70°$ and $90°$ corresponds to the incidences of the flow where the vortex breaks down. This corresponds to the flattening of L_s previously observed in figure 36. This connection between the normal force and L_s was previously detailed in (5.5) using a Riabouchinsky model of the recirculation.

Figure 38 shows the pitching moment M_z versus the angle of attack. For $Re = 0.15 \times 10^6$, M_z increases until $\alpha = 70°$ and drops to 0 at $\alpha = 90°$. For $Re = 1 \times 10^6$, the pitching moment increases until $\alpha = 30°$, has a local minimum at $\alpha = 50°$ and decreases again starting from $\alpha = 70°$. For $Re \geqslant 1.5 \times 10^6$, has only one maximum M_z between $\alpha = 40°$ and $\alpha = 50°$. The increasing pitching moment correlates with the increasing asymmetry of L_s and Γ_v in the axial direction (figures 36 and 21).

5.8.2. *Relation between loads and topology of recirculation*

As discussed in § 5.7, a balance between the shear stress on the boundary of the cavity and the suction on the wall of the spheroid can be expressed as $f_y(x) = \int_{\mathcal{S}} \tau_s \propto L_s \tau_s$ where $f_y(x)$ is the linear force such that $F_y = \int_0^L f_y(x) \mathrm{d}x$. That expression can be simplified as $(1/2)D(p_{wall} - p^\infty) = \tau_s L_s$ (Roshko 1993) assuming that the fluid boundary is an inviscid streamline of constant velocity and pressure. This assumption is not valid in any cavity formed in the lee of the spheroid because constant velocity and pressure implies constant stagnation pressure, which is not the case in this study. In the proto-vortex and 3-D

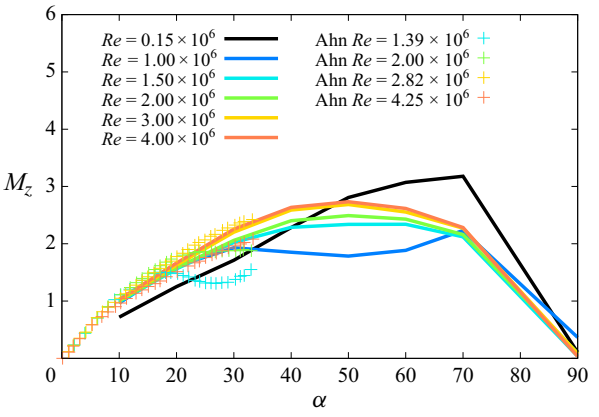

Figure 38. Pitching moment coefficient M_z versus angle of attack α for all six Reynolds numbers. The dotted lines are experimental results from Ahn (1992).

vortex states, the stagnation pressure is constant at $P_s = 0.49P_s^\infty$ along the separated shear layer but has higher values in the vicinity of the meridian plane. In the recirculating wake case, the 2-D stagnation point is located in a region of lower stagnation pressure. However, the definition of the recirculation area and the vortex based on stagnation pressure allow for a similar statement (Plasseraud & Mahesh 2024*a*).

At any axial location where a coherent vortex is formed, the pressure contribution of the in-plane vortex-induced force is zero by Crocco's equation: $f_y^{vortex}(x) = \int_{\mathcal{A}} \langle \boldsymbol{u} \times \boldsymbol{\omega} \rangle = \int_{\mathcal{A}} (\nabla P_s + \nabla \tau) = P_s^0 \int_{\mathcal{S}} \hat{n} + \int_{\mathcal{S}} \tau_s \cdot \hat{n} = \int_{\mathcal{S}} \tau_s \cdot \hat{n}$ where $\mathcal{A}$ is the 2-D area of the vortex at location x bounded by $\mathcal{S}$ of normal $\hat{n}$ and constant saddle stagnation pressure P_s^0. In addition, the shear stress can be approximated as $\int_{\mathcal{S}} \tau_s \cdot \hat{n} \approx r_0(\langle v'w' \rangle_r - \langle v'w' \rangle_l)$ where $_r$ and $_l$ refer to the left and right of the vortex boundary, respectively. Thus, the only contribution of vertical linear force from vortex comes from a left/right asymmetry in the turbulent stresses. If the vortex asymmetry is small, this term becomes small, and the force from the vortex is also small.

To assess the linear force from the total area of recirculation A_t, a similar argument can be made except that the isoline of stagnation pressure of that area is only constant in the fluid domain. On the wall, the value of stagnation pressure is equal to the pressure due to the no-slip condition, the pressure contribution to the vertical linear force can be reduced as $f_y^{recirculation}(x) = \int_{\phi_s}^{\phi_{max}} (0.49P_s^\infty - p^{wall}) d\phi$ where ϕ_{max} is the maximum azimuth of the recirculation on the wall. From this expression, the suction from the recirculation scales with the width of the recirculation. Equivalently, the vortex force from a region $\mathcal{S}$ of the fluid can be written in the inviscid limit as the integral of the Lamb vector $F = \int_{\mathcal{S}} \langle \boldsymbol{u} \times \boldsymbol{\omega} \rangle \mathrm{d}\mathcal{S} \approx \int_{\mathcal{S}} \nabla P_s \, \mathrm{d}\mathcal{S}$ (Saffman 1995). Note that this expression is equivalent to the Kutta–Joukowski theorem in the case of a vortex aligned with x and a force in the y direction, $\langle \boldsymbol{u} \times \boldsymbol{\omega} \rangle_y = \langle w \cdot \omega_x \rangle$. Interestingly, this expression involves the spanwise component of velocity, which explains why the linear force is not greater when the recirculation is the largest (generally at the tail of the spheroid) but when the separation azimuth is delayed and the transverse velocity is highest (midbody of the spheroid).

6. Conclusion

The flow around the prolate spheroid was studied for a wide range of Reynolds numbers and angles of attack. The separation of the boundary layer leads to a recirculation that is

in one of three states: proto-vortex, coherent vortex or recirculating wake. In the proto-vortex state, the recirculation is dominated by the axial component of velocity, and does not have a minimum of pressure. This state is prevalent at low angle of attack and in the early stage of flow separation. In the coherent vortex state, the recirculation forms a distinct vortex that turns the transverse components of velocity into axial velocity. The vortex was found to evolve in three stages: inception from proto-vortex, growth and decay. During the growth stage, the circulation in the coherent vortex increases with x, fed by a constant flux of vorticity at separation. Despite an axial increase in circulation, the average vorticity and axial flow rate decrease. This decrease is driven by a quadratic increase in the area of recirculation, which is a consequence of the squeezing of the vortex. In turn, this compression leads to a decrease in the overall swirl and strength of the vortex. The decrease of swirl and the decay of the vortex leads to an increase in the leeward side pressure and a topological change of the separation region as the flow becomes a recirculating wake. In this state, no coherent vortex is formed, instead, the cavity is bounded by a symmetric pair of decaying shear layer. An increase in the angle of incidence was found to correlate with a higher transverse flux of mass and vorticity, leading to a faster axial increase in size and circulation of the recirculating flow. This faster increase is correlated with an increase in lift, up to $\alpha = 70^\circ$ where the primary vortex pair loses coherence and the mean suction decreases. An increase in Reynolds number leads to a delayed separation and a closing of the separated sheet. This closing leads to a smaller recirculation area, a smaller vortex and a lower lift. For a fixed Reynolds number and angle of attack, the lift is higher for the first-half of the spheroid and decreases towards the tail. This helps explain the overturning pitching moment created by the vortex despite the nose/tail symmetry of the geometry. Maximum suction was not found at the location of highest circulation or where the recirculation area is the largest, but in regions of high swirl and vortex stretching. The current study helps to understand how the angle of attack and the Reynolds number affect boundary layer separation, recirculation and loads on the prolate spheroid. These dynamics are commonly found on other canonical flows such as cylinders, cones, delta wings and in more complex, practical applications such as aerial and underwater vehicles. The wide range of Reynolds numbers and angles of attack could help future investigations into flow control strategy, numerical simulation and experiment.

Acknowledgements. S. Prajapati, T. Leasca and Dr G. Wu for technical discussions; T. Kadambi and S. Ramesh for assistance in the meshing process. Preliminary results on the effects of Reynolds number and angle of attack are detailed in Plasseraud & Mahesh (2024*b*).

Funding. This work is supported by the United States Office of Naval Research (ONR) under ONR grant N00014-20-1-2717 with Dr P. Chang and Dr Y.L. Young as technical monitors. Computational resources for this work were provided through a United States Department of Defense (DoD) Frontier project of the High-Performance Computing Modernization Program (HPCMP) and the Engineer Research and Development Center (ERDC) of HPCMP.

Declaration of interests. The authors report no conflict of interest.

References

Ahn, S. 1992 An experimental study of flow over a 6 to 1 prolate spheroid at incidence. PhD thesis, Virginia Polytechnic Institute and State University.

Anderson, P.W. 1966 Considerations on the flow of superfluid helium. *Rev. Mod. Phys.* **38** (2), 298.

Aram, S., Shan, H. & Jiang, L. 2021 CFD analysis of boundary layer transition by passive tripping. In *AIAA Scitech 2021 Forum*. AIAA.

Aram, S., Shan, H., Jiang, L. & Atsavapranee, P. 2022 Numerical analysis of natural boundary layer transition and trip effect on inclined spheroid. In *AIAA Scitech 2022 Forum*. AIAA.

BARBER, K.M. & SIMPSON, R.L. 1990 Mean velocity and turbulence measurements of flow around a 6 : 1 prolate spheroid. Tech. Rep., Virginia Polytechnic Institute and State University.

BROWN, C.E., Jr. & MICHAEL, W.H. 1954 Effect of leading-edge separation on the lift of a delta wing. *J. Aeronaut. Sci.* **21** (10), 690–694.

CEBECI, T. & MEIER, H. 1987 Turbulent boundary layers on a prolate spheroid. In *19th AIAA, Fluid Dynamics, Plasma Dynamics, and Lasers Conference*. AIAA.

CHESNAKAS, C.J. & SIMPSON, R.L. 1994 Full three-dimensional measurements of the cross-flow separation region of a 6 : 1 prolate spheroid. *Exp. Fluids* **17** (1), 68–74.

CHESNAKAS, C.J. & SIMPSON, R.L. 1996 Measurements of the turbulence structure in the vicinity of a 3-D separation. *Trans. ASME.*

CHESNAKAS, C.J. & SIMPSON, R.L. 1997 Detailed investigation of the three-dimensional separation about a 6 : 1 prolate spheroid. *AIAA J.* **35** (6), 990–999.

CONSTANTINESCU, G.S., PASINATO, H., WANG, Y., FORSYTHE, J.R. & SQUIRES, K.D. 2002 Numerical investigation of flow past a prolate spheroid. *J. Fluids Engng* **124** (4), 904–910.

CRABBE, R. 1965 Flow separation about elliptic cones at incidence. In *AIAA 2nd Annual Meeting*. AIAA.

DU, Y. & ZAKI, T.A. 2025 Vorticity dynamics and drag for flows over a sphere and a prolate spheroid. *J. Fluid Mech.* **1015**, A9.

EL KHOURY, G.K., ANDERSSON, H.I. & PETTERSEN, B. 2010 Crossflow past a prolate spheroid at Reynolds number of 10 000. *J. Fluid Mech.* **659**, 365–374.

EL KHOURY, G.K., ANDERSSON, H.I. & PETTERSEN, B. 2012 Wakes behind a prolate spheroid in crossflow. *J. Fluid Mech.* **701**, 98–136.

FU, T.C., SHEKARRIZ, A., KATZ, J. & HUANG, T.T. 1994 The flow structure in the lee of an inclined 6 : 1 prolate spheroid. *J. Fluid Mech.* **269**, 79–106.

FUREBY, C. & KARLSSON, A. 2009 LES of the flow past a 6: 1 prolate spheroid. In *47th AIAA Aerospace Sciences Meeting including The New Horizons Forum and Aerospace Exposition*. AIAA.

GERMANO, M., PIOMELLI, U., MOIN, P. & CABOT, W.H. 1991 A dynamic subgrid-scale eddy viscosity model. *Phys. Fluids A* **3** (7), 1760–1765.

GOODY, M., SIMPSON, R.L. & ENGEL, M. 1998 Mean velocity and pressure and velocity spectral measurements within a separated flow around a prolate spheroid at incidence. In *36th AIAA Aerospace Sciences Meeting and Exhibit*. AIAA.

GRIFFIN, K.P., FU, L. & MOIN, P. 2021 General method for determining the boundary layer thickness in nonequilibrium flows. *Phys. Rev. Fluids* **6** (2), 024608.

GUO, P., KAISER, F. & RIVAL, D.E. 2023 Vortex-wake formation and evolution on a prolate spheroid at subcritical Reynolds numbers. *Exp. Fluids* **64** (10), 167.

HEDIN, P., BERGLUND, M., ALIN, N. & FUREBY, C. 2001 Large eddy simulation of the flow around an inclined prolate spheroid. In *39th Aerospace Sciences Meeting and Exhibit*. AIAA.

HORNE, W.J. & MAHESH, K. 2019*a* A massively-parallel, unstructured overset method for mesh connectivity. *J. Comput. Phys.* **376**, 585–596.

HORNE, W.J. & MAHESH, K. 2019*b* A massively-parallel, unstructured overset method to simulate moving bodies in turbulent flows. *J. Comput. Phys.* **397** (108790), 108790.

HUNT, J.C.R., WRAY, A.A. & MOIN, P. 1988 Eddies, streams, and convergence zones in turbulent flows. Studying turbulence using numerical simulation databases, 2. In *Proceedings of the 1988 summer program*, pp. 193–208. Center for Turbulence Research.

JEONG, J. & HUSSAIN, A.K.M.F. 1995 On the identification of a vortex. *J. Fluid Mech.* **285**, 69–94.

JIANG, F., ANDERSSON, H.I., GALLARDO, J.P. & OKULOV, V.L. 2016 On the peculiar structure of a helical wake vortex behind an inclined prolate spheroid. *J. Fluid Mech.* **801**, 1–12.

JIANG, F., GALLARDO, J.P. & ANDERSSON, H.I. 2014 The laminar wake behind a 6: 1 prolate spheroid at 45 incidence angle. *Phys. Fluids* **26** (11), 113602.

JOHNSON, T.A. & PATEL, V.C. 1999 Flow past a sphere up to a Reynolds number of 300. *J. Fluid Mech.* **378**, 19–70.

JOSEPHSON, B.D. 1965 Potential differences in the mixed state of type II superconductors. *Phys. Lett.; (Netherlands)* **16**, 242–243.

KIM, S.E., RHEE, SHIN & COKLJAT, D. 2003 Application of modern turbulence models to vortical flow around a prolate spheroid. In *41st Aerospace Sciences Meeting and Exhibit*. AIAA.

KROLL, T.B. & MAHESH, K. 2022 Large-eddy simulation of a ducted propeller in crashback. *Flow* **2**, E4.

KUMAR, P. & MAHESH, K. 2018 Large-eddy simulation of flow over an axisymmetric body of revolution. *J. Fluid Mech.* **853**, 537–563.

LEASCA, T.J.T., KROLL, T.B. & MAHESH, K. 2025 Large-eddy simulation of the tip vortex flow in a ducted propulsor. *J. Fluid Mech.* **1010**, A51.

LEE, M. & HO, C.-M. 1990 Lift force of delta wings. *Appl. Mech. Rev.* **43**, 9.

LEVY, Y., DEGANI, D. & SEGINER, A. 1990 Graphical visualization of vortical flows by means of helicity. *AIAA J.* **28** (8), 1347–1352.
LILLY, D.K. 1992 A proposed modification of the Germano subgrid-scale closure model. *Phys. Fluids A* **4** (3), 633.
MAHESH, K., CONSTANTINESCU, G. & MOIN, P. 2004 A numerical method for large-eddy simulation in complex geometries. *J. Comput. Phys.* **197** (1), 215–240.
MOFFATT, H.K. & TSINOBER, A. 1992 Helicity in laminar and turbulent flow. *Annu. Rev. Fluid Mech.* **24** (1), 281–312.
MORRISON, J., PANARAS, A., GATSKI, T. & GEORGANTOPOULOS, G. 2003 Analysis of extensive cross-flow separation using higher-order RANS closure models. In *21st AIAA Applied Aerodynamics Conference*. AIAA.
MORSE, N. & MAHESH, K. 2021 Large-eddy simulation and streamline coordinate analysis of flow over an axisymmetric hull. *J. Fluid Mech.* **926**, A18.
PLASSERAUD, M., KUMAR, P. & MAHESH, K. 2023 Large-eddy simulation of tripping effects on the flow over a 6 : 1 prolate spheroid at angle of attack. *J. Fluid Mech.* **960**, A3.
PLASSERAUD, M. & MAHESH, K. 2024*a* Definition of vortex boundary using stagnation pressure. *Phys. Rev. Fluids* **9** (11), 114701.
PLASSERAUD, M. & MAHESH, K. 2024*b* Reynolds number and angle of attack effects on the flow over a 6 : 1 prolate spheroid. In Proceedings of the 35th Symposium on Naval Hydrodynamics. Symposium on Naval Hydrodynamics.
REYNOLDS, A.J. 1962 Similarity in swirling wakes and jets. *J. Fluid Mech.* **14** (2), 241–243.
RHEE, S.H. & HINO, T. 2002 Numerical simulation of unsteady turbulent flow around maneuvering prolate spheroid. *AIAA J.* **40** (10), 2017–2026.
RIABOUCHINSKY, D. 1921 On steady fluid motions with free surfaces. *Proc. Lond. Math. Soc.* **2** (1), 206–215.
ROSHKO, A. 1993 Perspectives on bluff body aerodynamics. *J. Wind Engng Indust. Aerodyn.* **49** (1–3), 79–100.
RUBINO, G. 2021 Laminar-to-turbulence transition modeling of incompressible flows in a rans framework for 2d and 3d configurations. PhD thesis, Ecole Centrale de Nantes.
SAFFMAN, P.G. 1995 *Vortex Dynamics*. Cambridge University Press.
SCOTT, N. & DUQUE, E. 2004 Unsteady Reynolds-averaged Navier–Stokes predictions of the flow around a prolate spheroid. In *42nd AIAA Aerospace Sciences Meeting and Exhibit*. AIAA.
STRANDENES, H., JIANG, F., PETTERSEN, B. & ANDERSSON, H.I. 2019 Near-wake of an inclined 6 : 1 spheroid at Reynolds number 4000. *AIAA J.* **57** (4), 1364–1372.
TANEDA, S. 1956 Experimental investigation of the wake behind a sphere at low Reynolds numbers. *J. Phys. Soc. Japan* **11** (10), 1104–1108.
TRUESDELL, C. 1954 *The Kinematics of Vorticity*. Indiana University Press.
VERMA, A. & MAHESH, K. 2012 A Lagrangian subgrid-scale model with dynamic estimation of Lagrangian time scale for large eddy simulation of complex flows. *Phys. Fluids* **24** (8), 085101.
WETZEL, T.G. 1996 Unsteady flow over a 6: 1 prolate spheroid. *PhD thesis*, Virginia Polytechnic Institute and State University.
WIKSTRÖM, N., U., S., ALIN, N. & FUREBY, C. 2004 Large eddy simulation of the flow around an inclined prolate spheroid. *J. Turbul.* **5** (1), 029.
WILLIAMSON, C.H.K. 1996 Vortex dynamics in the cylinder wake. *Annu. Rev. Fluid Mech.* **28**, 477–539.
WU, J.Z., LU, X.Y. & ZHUANG, L.X. 2007 Integral force acting on a body due to local flow structures. *J. Fluid Mech.* **576**, 265–286.
XIAO, Z., ZHANG, Y., HUANG, J., CHEN, H. & FU, S. 2007 Prediction of separation flows around a 6 : 1 prolate spheroid using RANS/LES hybrid approaches. *Acta Mechanica Sinica* **23** (4), 369–382.